

Two liquid states of distinguishable helium-4: the existence of another non-superfluid frozen by heating

Momoko Tsujimoto* and Kenichi Kinugawa†

*Department of Chemistry, Graduate School of Humanities and Sciences,
Nara Women's University, Nara 630-8506, Japan*

We show that there can exist two liquid states in distinguishable helium-4 (^4He) obeying Boltzmann statistics by path integral centroid molecular dynamics (CMD) simulations. This is an indication of quantum liquid polyamorphism induced by nuclear quantum effect. For 0.08–3.3 K and 1–500 bar, we extensively conducted the isothermal-isobaric CMD simulations to explore not only possible states and state diagram but the state characteristics. The distinguishable ^4He below 25 bar does not freeze down to 0.1 K even though it includes no Bosonic exchange effect and therefore no Bose condensation. One liquid state, low quantum-dispersion liquid (LQDL), is nearly identical to normal liquid He-I of real ^4He . The other is high quantum-dispersion liquid (HQDL) consisting of atoms with longer quantum wavelength. This is another non-superfluid existing below 0.5 K or the temperatures of LQDL. The HQDL is also a low-entropy and fragile liquid to exhibit, unlike conventional liquids, rather gas-like relaxation of velocity autocorrelation function, while there the atoms diffuse without noticeable contribution from quantum tunneling. The LQDL-HQDL transition is not a thermodynamic phase transition but a continuous crossover accompanied by the change of the expansion factor of quantum wavelength. Freezing of HQDL into the low quantum-dispersion amorphous solid occurs by heating from 0.2 to 0.3 K at 40–50 bar, while this P - T condition coincides with the Kim-Chan normal-supersolid phase boundary of real ^4He . The obtained state diagram was compared with that of the confined subnano-scale ^4He systems where Bosonic correlation is considerably suppressed.

I. INTRODUCTION

Is it a true postulation that every substance should freeze into its solid phase as it is cooled down toward absolute zero temperature? While classical systems inevitably freeze by losing kinetic energy proportional to temperature, anti-freezing of quantum systems is benefited by promotion of atomic diffusivity due to increasing quantum atomic fluctuation down to zero temperature. Indeed, we know an exceptionally non-freezing quantum substance, helium-4 (^4He), which retains the superfluid (He-II) phase which never freezes down to zero temperature under atmospheric pressure. The cause of superfluidity includes: (i) the nuclear quantum effect (NQE), i.e., the atomic wave nature parametrized as the de Broglie thermal wavelength $\lambda_{\text{dB}} := \hbar\sqrt{2\pi/mk_{\text{B}}T}$ (m is the atomic mass and k_{B} is the Boltzmann constant), (ii) the weakness of the van der Waals interatomic forces, and (iii) the atomic indistinguishableness due to the Bosonic permutation [1]. Primitively, the λ -type isobaric heat capacity C_P at the transition between normal liquid (He-I) and He-II of ^4He is explained in terms of the Bose-Einstein condensation (BEC) of ideal Bose gas [2–4]. This leads to a conventional understanding that the Bose statistics is the key to the λ transition and causes the BEC through which non-freezing of this quantum substance is achieved. Then, if there were solely the

NQE and no Bosonic exchange were imposed on atoms, could such a distinguishable ^4He model avoid freezing to retain the normal liquid phase when cooled? According to Feynman [1], it was argued that there was no difference between the ground state wave function of an ensemble of Bosons and of distinguishable particles [5]. This indicates that distinguishable ^4He at atmospheric pressure is liquid at $T = 0$ as is the Bosonic system. As discussed [5], in the textbooks [1, 6], the non-freezing property of ^4He was explained by considering only the two factors (i) the NQE of individual atoms and (ii) the weak interatomic forces [6]. However, Boninsegni et al. reported that the third factor, (iii) the Bosonic exchange among N atoms, was indispensable to retaining the non-freezing property by being in superfluid state; the crystal of distinguishable ^4He melted by introducing the Bosonic correlation [5]. Therefore, the state of distinguishable ^4He would not always be the same as that of the Bosonic counterpart in general. However, for a wider range of pressure and non-zero low temperature, it has not yet been completely explored what kind of states emerges by the sole NQE in distinguishable ^4He .

The non-freezing tendency of a quantum substance might be reflected to the ease of residual diffusion [7] of atoms in its quenched glassy solid. In this connection, Markland et al. conducted the discretized path integral simulations based on the quantum-classical isomorphism, where quantum atoms are expressed as classical ring polymers (necklaces), to show the reentrant behavior of self-diffusion coefficient D in the glassy solid of a binary Lennard-Jones model. In their study, increasing the quantumness parameter $\Lambda^* := \hbar/\sqrt{mk_{\text{B}}T\sigma^2}$ (σ is the closest interatomic distance) caused the transi-

* Present address: KYOCERA Communication Systems Co., Ltd., Takeda-tobadono, Fushimi-ku, Kyoto 612-8450, Japan.

† Author to whom correspondence should be addressed. kinugawa@cc.nara-wu.ac.jp

tion from a glass state involving trapped configurations of atomic necklaces (called *trapped regime*) to another state with stretched configurations of atoms (*tunneling regime*) [8, 9]. As Λ^* increased, D once decreased in the former regime but it turned to increase in the latter [8, 9]. This also suggested a tendency toward inverse melting (or *melting by cooling*) of this quantum system [9]. In fact, such an atomic tunneling between local potential minima explains the linear temperature dependence of heat capacity in low-temperature glasses [10, 11].

The existence of more than one states in liquids or glasses is called polyamorphism [12, 13], which is, for example, observed for classical *fragile* liquids [14] such as water [15, 16] and phosphorous [17]. The existence of two liquid states, He-I and He-II, in ^4He is certainly an example of liquid polyamorphism. However, the polyamorphism of the other quantum systems has rarely been discovered so far [18–20]. Recently, our path integral centroid molecular dynamics (CMD) simulations showed a quantum polyamorphism of compressed distinguishable ^4He glass above 3 K [21]. In good accordance with the two regimes reported by Markland et al. [8, 9], compressed distinguishable ^4He also involved two glass states [21]. The two states were distinguished by the difference in atomic quantum wavelength λ_{quantum} which is equivalent to two times *radius of gyration* of atomic necklaces [21]. Then we call the two states, depending on λ_{quantum} , the low quantum dispersion amorphous solid (LQDA) and the high quantum dispersion solid (HQDA) [21] [22]. The LQDA and HQDA are equivalent to the trapped and the tunneling regimes in the quantum Lennard-Jones model [8, 9], respectively. The LQDA-HQDA transition was reversibly caused by varying temperature or pressure, while this was akin to the coil-globule transition of classical polymers [23–31]. In accordance with the reports by Markland et al. [8, 9], increasing the quantumness parameter by compression or cooling promoted the residual diffusion of atoms in the HQDA state. Thus, the NQE is certainly a cause of the polyamorphism and the enhancement of atomic diffusivity in these quantum glasses.

For distinguishable ^4He , we anticipate that a liquid polyamorphism may occur as the counterpart of observed glass polyamorphism [21], since the glass structure is produced by quenching the liquid configurations. Another reason for this anticipation is that an extrapolation of the LQDA-HQDA boundary line on the state diagram [21] (which will be shown later in Fig. 12 in this paper) would reach a particular region ($T \simeq 0.2$ K and $P \simeq 26$ bars) at which Kim and Chan experimentally observed the torsional oscillation anomaly suggesting the existence of *supersolid* [32]. Although subsequent researches provided more freedom in the interpretation of their measured results [33], some unusual state must be emerging in real ^4He at this P - T condition. The third reason is that the experimental melting curves of both ^4He and ^3He are slightly downward convex possessing shallow minima on the P -vs- T plane (^4He : 0.8 K and 26 bars; ^3He : 0.3 K and 29 bar) [34]. In fact, the existence of an minimum

of melting curve is a thermodynamical implication of liquid polyamorphism [12, 13, 35]. In general, when a state point on the P - T plane moves across a convex melting curve, even an inverse freezing (freezing by heating) or an inverse melting (melting by cooling) occurs [36–41]. For these reasons, it is expected that two liquid states emerge in distinguishable ^4He including the occurrence of inverse melting. Nevertheless, this issue remains unresolved, while the phase diagram of distinguishable ^4He has never been revealed except for a presumed outline [5].

Motivated by these questions, in the present study we started to undertake the isothermal-isobaric CMD simulation of the distinguishable ^4He model. The surveyed range spanned 0.08–3.3 K and 1–500 bar, involving 357 mesh points which covered the P - T conditions of He-I, He-II, and solid phase of real ^4He . This is an ideal model to investigate what kind of states appears in quantum liquid as a result of the sole NQE without inclusion of Bosonic exchange correlation.

This paper is organized as follows. Section II describes the CMD simulation method. The results of the isothermal compression simulation are described in Sec. III. At the beginning of this section, we provide the state diagram on the P - T plane as a summary of the isothermal compression simulation. And then we show the results of static and dynamic properties supporting the conclusion of this state diagram. In Sec. IV, we present the detailed analysis on the basis of the state diagram. The discussions are given in Sec. V. Finally, we describe the conclusions in Sec. VI. Appendix provides the results of another CMD simulation conducted to examine the occurrence of inverse freezing, and also gives comparisons of the state diagram with that of the real confined ^4He systems and reported *supersolid*.

In the Supplementary Material, we provide a substantial amount of additional figures and data.

II. METHOD

A. Isothermal-isobaric CMD

To explore the phase equilibrium of substances, the investigation should be undertaken for an isothermal-isobaric ensemble because thermodynamic phase is uniquely determined under a given condition of P and T [42]. For a quantum system, the discretized path integral representation provides the quantum-classical isomorphism that the partition function of a quantum system consisting of N quantum atoms is equivalent to that of a classical system composed of N necklaces (ring polymers); each of necklaces consists of N_b beads connected with the springs [43]. Then the partition function of an isothermal-isobaric ensemble of N distinguishable ^4He atoms at inverse temperature $\beta = (k_B T)^{-1}$ and external pressure P_{ex} is then

$$\Delta_{NPT} = \frac{1}{v} \int dV \exp(-\beta P_{\text{ex}} V) \int \cdots \int \prod_{i=1}^N d\mathbf{r}_{ci} \rho_c(\{\mathbf{r}_{ci}\}), \quad (1)$$

where v is a certain quantity of volume [44] and ρ_c is the centroid density,

$$\rho_c(\{\mathbf{r}_{ci}\}) = \frac{1}{N!} \lim_{N_b \rightarrow \infty} \left(\frac{m}{2\pi\beta\hbar^2} \right)^{\frac{3NN_b}{2}} \int \cdots \int \prod_{i=1}^N \prod_{j=1}^{N_b} d\mathbf{r}_i^{(j)} \delta(\mathbf{r}_{ci} - \bar{\mathbf{r}}_i) \exp \left[-\beta H_{\text{system}}(\{\mathbf{r}_i^{(j)}\}) \right]. \quad (2)$$

Here, the system Hamiltonian H_{system} is [43]

$$H_{\text{system}}(\{\mathbf{r}_i^{(j)}\}) = \sum_{i=1}^N \sum_{j=1}^{N_b} \frac{1}{2} k_s \left(\mathbf{r}_i^{(j)} - \mathbf{r}_i^{(j+1)} \right)^2 + \frac{1}{N_b} \Phi(\{\mathbf{r}_i^{(j)}\}), \quad (3)$$

N_b is the discretization number (the Trotter number), m is the atomic mass, $\mathbf{r}_i^{(j)}$ is the position of the j -th bead (i.e., the atomic position at imaginary time $\tau_j = j\beta\hbar/N_b$ ($0 < \tau_j \leq \beta\hbar$)) of the i -th atom, $\bar{\mathbf{r}}_i$ is the imaginary-time averaged position, $\bar{\mathbf{r}}_i = N_b^{-1} \sum_{j=1}^{N_b} \mathbf{r}_i^{(j)}$, k_s is the Hooke constant, $k_s = mN_b/\beta^2\hbar^2$, and Φ is the system potential arising from pairwise interatomic interactions. Since the cyclic boundary condition $\mathbf{r}_i^{(N_b+1)} = \mathbf{r}_i^{(1)}$ is imposed, the isomorphic classical system consists of N necklaces where N_b beads are sequentially connected through the springs with the Hooke constant k_s . Therefore, the springs become looser as the temperature falls.

On the basis of this representation, we conducted the isothermal-isobaric Nosé-Hoover-chain-Andersen-type normal-mode CMD (NMCMD) simulations for a bulk ^4He system of 256 atoms contained in a cubic box under the periodic boundary condition. The simulation technique was the same as our recent work [21]. The pair He-He interatomic potential was Aziz's HFD-B3-FCI1 type [45], which was also adopted in our recent study [21, 46]. The centroid equation of motion for an isothermal-isobaric ensemble is

$$m\ddot{\mathbf{r}}_{ci} = \mathbf{F}_{ci} - m\dot{\xi}_1 \dot{\mathbf{r}}_{ci} - \frac{m}{N} \dot{\epsilon} \ddot{\mathbf{r}}_{ci}, \quad i = 1, 2, \dots, N, \quad (4)$$

where $\dot{\xi}_1$ is the velocity of the first layer of the Nosé-Hoover chain thermostat, $\dot{\epsilon}$ is the velocity of the Andersen barostat, and \mathbf{F}_{ci} is the interatomic force arising from Φ ,

$$\begin{aligned} \mathbf{F}_{ci} &= - \frac{\partial H_{\text{system}}(\{\mathbf{r}_i^{(j)}\})}{\partial \mathbf{r}_{ci}} \\ &= - \frac{1}{N_b} \sum_{j=1}^{N_b} \frac{\partial \Phi(\{\mathbf{r}_i^{(j)}\})}{\partial \mathbf{r}_i^{(j)}} \equiv \frac{1}{N_b} \sum_{j=1}^{N_b} \mathbf{f}_i^{(j)}. \end{aligned} \quad (5)$$

Equation (4) was numerically solved together with the equations of motion of the normal-mode-transformed bead coordinates by use of the NMCMD algorithm [21]. The centroid time increment Δt_{MD} was taken as 0.1 fs. The time increment for the normal-mode propagation

was taken equal to Δt_{MD} , while the effective period [21] of the non-centroid normal-modes was set at 100 fs.

The system pressure was evaluated via the virial theorem [47]. The system kinetic energy K was evaluated from the centroid-reference virial estimator [48–50],

$$\begin{aligned} K &= \sum_{i=1}^N K_i \\ &= \sum_{i=1}^N \left(\frac{3}{2} k_B T - \frac{1}{2N_b} \left\langle \sum_{j=1}^{N_b} (\mathbf{r}_i^{(j)} - \mathbf{r}_{ci}) \cdot \mathbf{f}_i^{(j)} \right\rangle \right). \end{aligned} \quad (6)$$

In Eq. (6), the contributing term K_i is not dependent solely on atom i since it consists of the averaged virial terms including interatomic forces $\mathbf{f}_i^{(j)}$.

In our previous study [21], we confirmed that the CMD simulation method accurately reproduced the measured isotherms of V vs P and of the internal energy U vs P for real ^4He in the temperature range where the Bose statistics is negligible.

B. Check of the Trotter number dependence

First, we checked the Trotter number N_b dependence of energetic properties. The results of the energetic properties at 0.1 K are shown in Fig. SA-1 in the Supplementary Material. In this figure, we can see a fair convergence of the energetic properties for $N_b \geq 500$, so that we adopted N_b as 500 in all the simulations in the present study. Figure SA-2 in the Supplementary Material shows the Trotter number dependence of energy-temperature relations obtained from the CMD simulation at 1 bar. In this figure, the energetic properties for $T \lesssim 0.1$ K depend fairly on N_b and the convergence of estimated energy values is not good. For $T \lesssim 0.1$ K, remarkable dropping of H , U , and Φ is observed for $500 \leq N_b \leq 2000$, though K converges fairly well. We see that Φ , U , and H were evaluated low too much at $T \lesssim 0.1$ K when we adopted the setting of $N_b \leq 2000$. However, there is a symptom that the temperature dependence plot of each energy in

the case of $N_b = 3000$ is likely to converge asymptotically to a horizontal value as $T \rightarrow 0$ K. The plot looks like a slight S-curve in the range of $0.01 \leq T \leq 0.1$ K. If we adopted the Trotter number as $N_b > 3000$, more accurate results would be obtained even for $T \lesssim 0.1$ K. Although the low temperature properties at $T < 0.1$ K are intriguing, we would rather save this subject for a future work. As for the results shown in this paper, we need to be careful that the thermodynamic properties at $T \lesssim 0.1$ K in this work, where we set $N_b = 500$, contains this degree of inaccuracy. The N_b -dependence of other properties is also shown in Figs. SA-3 and SA-4 in the Supplementary Material; this issue is discussed in Secs. III C and III D.

C. Survey of pressure-temperature points by isothermal compression

We surveyed possible states at 357 P - T mesh points in the range of $0.08 \leq T \leq 3.3$ K and $1 \leq P \leq 500$ bar; Figure SA-5 in the Supplementary Material shows these points plotted on the P - T plane. The procedure of the CMD simulation, shown schematically in Fig. SA-6 in the Supplementary Material, is as follows:

(1) First, the system was equilibrated at 3.3 K and 1 bar, and then it was stepwise cooled toward 0.08 K, keeping the pressure at 1 bar. In this isobaric procedure, CMD was carried out spanning 100,000 steps (10 ps) at each temperature, and then the set temperature was switched to the next lower temperature. Then the system was further equilibrated spanning 200,000 steps (20 ps), followed by another 200,000 steps' production run, from which the physical properties at 1 bar given in the following sections were calculated.

(2) Next, the isothermal compression was started from the end configuration of the 1 bar production run at each temperature. At each temperature in the range of 0.08-3.3 K, the set hydrostatic pressure was increased to the next higher value stepwise toward 500 bar. The pressure was kept constant during each time interval of 50,000 steps, and increased at the end of each interval. At each P - T point we further conducted 150,000 steps' (15 ps) production run. The physical properties for $P > 1$ bar shown in the following sections were evaluated from each production run.

III. RESULTS

In this section, we show the results of the CMD simulations. First, in Sec. III A, we present the P - T state diagram which was derived from the computational results. In Secs. III B-III E, we provide the results evidencing the conclusion of state diagram, while the criterion for the identification of states is described in Sec. III F. Finally, the examination of atomic tunneling and the velocity autocorrelation function are presented in Secs. III G and

III H, respectively.

A. State diagram

Figure 1 shows the P - T state diagram derived from the computational results in the present study, together with our previous results for higher P - T conditions [21]. Similar to the compressed conditions [21], we can observe the existence of two glassy states, LQDA and HQDA, also in the P - T range of the present study. Moreover, we can see the existence of two liquid states: low quantum dispersion liquid (LQDL) and high quantum dispersion liquid (HQDL). They are distinguished from each other mainly by the difference in quantum dispersion of atoms; the characteristics of these two liquid states are described in later subsections. The system at each P - T point retained its state throughout the simulation and no transition to another state was observed. Evidently, LQDA and HQDA should be metastable states which must eventually reach the crystalline state at an equilibrium even though we observed no state changes during the simulation. As LQDL exists also at P - T region of He-I at temperatures higher than λ -transition line, it is considered as being nearly identical to He-I of real ^4He . Further analysis regarding the state diagram will be described in Sec. IV.

For visual understanding, in Fig. 2 we show the snapshots of typical instantaneous configurations of LQDL and HQDL at 1 bar. Those for 40 bar are also shown in Fig. SA-7 in the Supplementary Material. In these figures, we find that the LQDA consists of localized necklaces representing low quantum dispersion (LQD) of ^4He atoms, while HQDA involves stretched necklaces representing high quantum dispersion (HQD) of atoms. However, the border of the two states is visually ambiguous.

B. Thermodynamic properties

Figures 3 and 4 show the temperature dependences of molar volume V and enthalpy H , respectively. We provide the complete set of data of the H - T plot over the entire range of 1-500 bar in Fig. SA-8 in the Supplementary Material, while the temperature dependences of K , U , and Φ are shown in Figs. SA-9, SA-10, and SA-11, respectively. In Figs. 3 and 4, we can see no discontinuity in each isobar of V - T and H - T plots, so that there is no evidence to support the existence of the first-order phase transition. In Fig. 3, we can see that some curves have negative slopes on the occasion of the HQDL \rightarrow LQDL or the HQDA \rightarrow LQDA transition. In contrast, in Fig. 4, each H - T curve is an increasing monotonous function of T , i.e., $(\partial H / \partial T)_P = C_P > 0$ (or $\Delta H > 0$ for heating) over the whole temperature range. Therefore, at a given pressure, HQDL existing at lower temperatures has lower entropy than LQDL or LQDA at higher temperatures, according to the relation $\Delta S = \int C_P dT / T$.

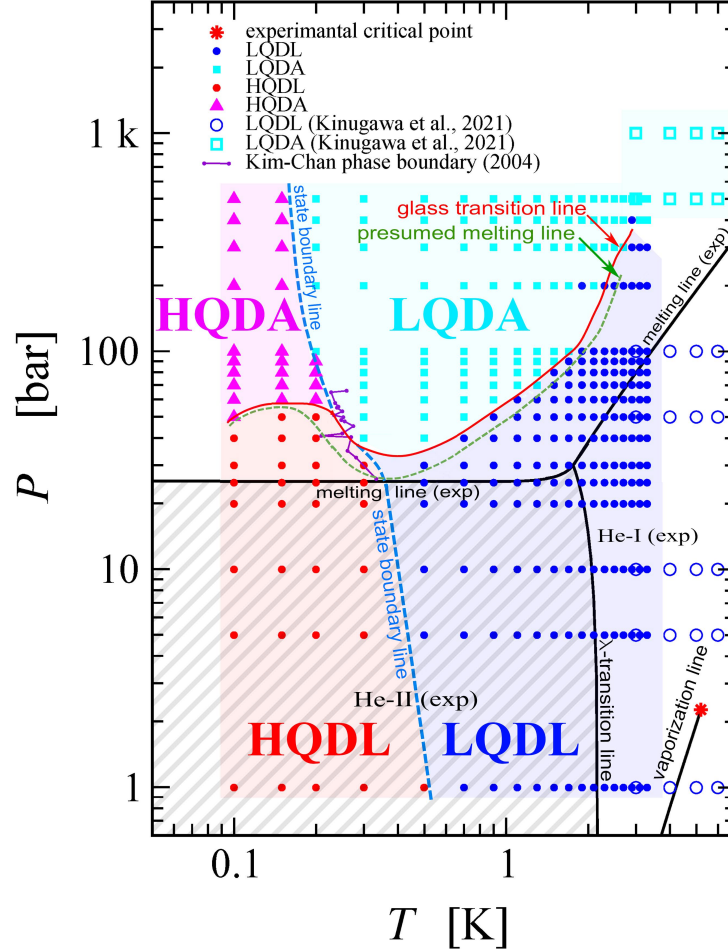


FIG. 1. The state diagram of distinguishable ${}^4\text{He}$ obtained from the isothermal compression by the CMD simulation. The points at 1 bar were obtained from the isobaric cooling from the state at 3.3 K. LQDL (blue): low quantum dispersion liquid; HQDL (red): high quantum dispersion liquid; LQDA (cyan): low quantum dispersion amorphous solid (metastable); HQDA (magenta): high quantum dispersion amorphous solid (metastable). Black solid lines are the experimental phase boundary lines of real ${}^4\text{He}$. Experimentally, He-I and He-II (gray slant stripe) exist at higher and lower temperatures than λ transition line (black), respectively, while the crystalline solid phase exists at pressures higher than the melting curve (black). The open symbols denote the states obtained from the isothermal compression in our previous study [21]. The points of “LQDL (Kinugawa et al., 2021)” [21] includes those of supercritical fluid (SCF) state with low quantum dispersion, existing beyond the critical point (red star). The melting line (dashed green line) is presumed to be located at lower pressures than the glass transition line (red line) because of overpressurization. The Kim-Chan phase boundary denotes the locus of the emergence of non-classical rotational inertia which then suggested the existence of *supersolid* at lower temperatures below this boundary [32]; see Appendix B.

In Fig. 4, the slope of the H - T plot, C_P , is larger at lower temperatures. For example, the C_P at 1 bar obtained from the curve fitting of the H - T relation is shown in Fig. SA-12 in the Supplementary Material. In this figure, we cannot see any indication of such C_P maximum as the λ -type peak in real ${}^4\text{He}$ and the cusp in the ideal Bose gas [4]. Therefore, there are no evidences for supporting the second-order phase transition between LQDL and HQDL. Consequently, each isobaric transition of HQDL-LQDL, HQDL-LQDA, and HQDA-LQDA is considered as a continuous crossover, not the thermodynamic phase transition.

There is a remarkable drop of H at $T \lesssim 0.1$ K in Fig. 4, and equivalently, one sees the divergent increase of C_P at the lowest temperature edge ($T \lesssim 0.1$ K) in Fig. SA-12 in the Supplementary Material. This is an artifact due to the insufficient N_b (Sec. II B). Though the computed values of, e.g., energetic properties, near 0.1 K are not completely accurate, the bulk of this work is hardly affected by the inaccuracy emerging at $T \lesssim 0.1$ K. As described in Sec. II B, when we adopted the Trotter number $N_b = 3000$, which should yield more accurate results, the H - T plot within $0.01 < T < 0.1$ K exhibited a symptom of slight S-curve with a subtle inflection point at ~ 0.02 K

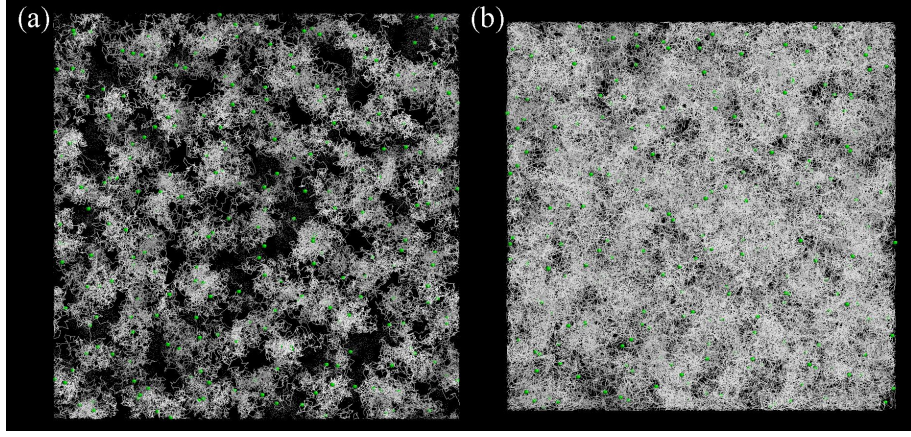


FIG. 2. The xy -projected snapshots of the configuration of the ^4He atomic necklaces and centroids. (a) low quantum dispersion liquid (LQDL) state at 1 bar and 1.5 K; (b) high quantum dispersion liquid (HQDL) state at 1 bar and 0.3 K. Green spheres and white ones denote the centroids and the beads, respectively. The drawn scales of the centroids and the beads are arbitrary.

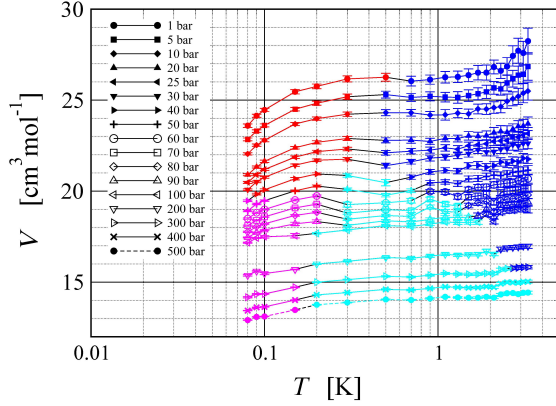


FIG. 3. The molar volume vs temperature. The lines denote isobars. The colors of the symbols are the same as those displayed in Fig. 1: LQDL (blue), LQDA (cyan), HQDL (red), and HQDA (magenta).

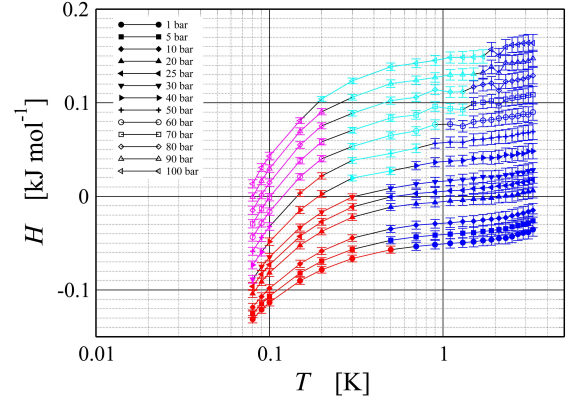


FIG. 4. The enthalpy vs temperature. The lines denote isobars. The colors of the symbols are the same as those displayed in Fig. 1: LQDL (blue), LQDA (cyan), HQDL (red), and HQDA (magenta).

(see Fig. SA-2(e) in the Supplementary Material). Then, the C_P may have a maximum at this temperature, and this would possibly imply another state transition. However, we do not draw a conclusion at present; this subject will be resolved in a future study which must demand very heavy computation with enormous N_b .

Figure 5 shows the volume dependence of kinetic energy K together with the experimental relation of real bulk ^4He . The experimental data points [51] of He-I, He-II, and solid phase likely lie on a single universal line, irrespective of temperature. The data points of the LQD states in the present work tends to gather to the vicinity of this universal curve, whereas those of the HQD states are clearly deviated from it and exhibit remarkable temperature dependence. This issue will be discussed in Sec. VB

C. Radial distribution functions

The radial distribution functions (RDFs) at selected P - T points are shown in Fig. 6, while the complete set of RDFs is shown in Figs. SB-1 and SB-2 in the Supplementary Material. In both the bead-bead RDF g_{bb} and the centroid-centroid RDF g_{cc} , we can recognize broad distributions, indicating that the system is in a liquid or glass state and denying the existence of crystalline order at all P - T conditions. However, in Fig. 6(b) and Fig. SB-1 in the Supplementary Material, the g_{cc} exhibits remarkable structural change due to the LQD-HQD state transition occurring in the range of 0.15-0.7 K. The peaks in g_{cc} of the HQD states are collapsed and there is non-zero distribution penetrated into $r \sim 0$ Å. However, this is not unnatural because the interatomic forces are not

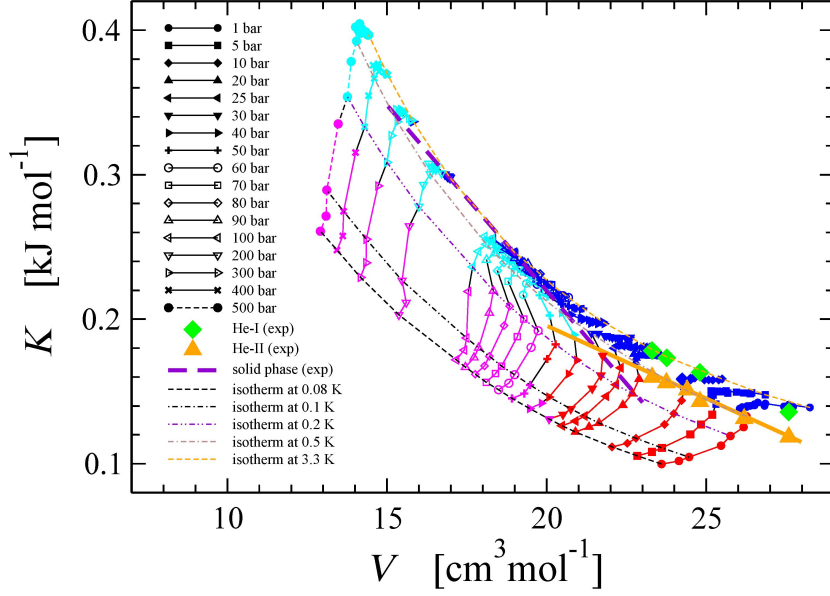


FIG. 5. The kinetic energy vs molar volume. LQDL (blue), LQDA (cyan), HQDL (red), and HQDA (magenta). All the experimental data are cited from Fig. 16 of Ref. 51; the measured temperature of normal fluid (He-I) and superfluid (He-II) spans $2.1 \leq T \leq 2.3$ K and $0.045 \leq T \leq 0.075$ K, respectively [51].

directly exerted on the centroid positions on which atoms do not exist. Since the profile of g_{bb} does not change significantly even on the occasion of the LQD-HQD state transition, structural change can be hardly detected by diffraction experiments, in spite of drastic change in the g_{cc} . In fact, the non-zero distribution at $r \sim 0$ Å in g_{cc} is also characteristic of the HQDA of compressed ^4He glass [21] and the classical ring polymer systems [52, 53].

We show the g_{cc} at 1 bar with $N_b = 500, 1500$, and 2000 in Fig. SA-4 in the Supplementary Material. For each of N_b , we can see that the LQD-HQD structural transition occurred at 0.5-0.7 K; the structure of HQD state is characterized by non-zero distribution of g_{cc} at the distances shorter than the first peak. Consequently, the occurrence of the LQD-HQD transition is not artificially caused by the insufficiency of N_b but attributed to an essential property of the system.

D. Quantum wavelength and expansion factor

To quantify the spatial extension of atomic necklaces, i.e., the degree of quantum dispersion, we evaluated quantum wavelength [21, 46] λ_{quantum} from the square root of the imaginary-time mean square displacements (IMSD) [54]. Namely, the IMSD at imaginary time

$\tau_n = n\beta\hbar/N_b$ is

$$R_{\text{IMSD}}^2(\tau_n) = \frac{1}{N} \sum_{i=1}^N \langle |\mathbf{r}_i^{(j+n)} - \mathbf{r}_i^{(j)}|^2 \rangle_j, \quad (7)$$

$$0 < \tau_n \leq \beta\hbar,$$

from which we estimated the quantum wavelength λ_{quantum} defined as

$$\lambda_{\text{quantum}} = \sqrt{R_{\text{IMSD}}^2(\beta\hbar/2)}. \quad (8)$$

The IMSD exhibits a semiarc-like curve as a function of τ_n [21, 46, 54]. The λ_{quantum} denotes an effective diameter of atomic necklaces and corresponds to twice the *radius of gyration* R_g in polymer physics terminology [55]. Figure 7 shows the temperature dependence of λ_{quantum} . At each pressure, λ_{quantum} tends to increase with lowering temperature. The HQDL exhibits significantly longer λ_{quantum} than the closest distances observed as the first peaks in g_{bb} in Fig. 6(a). For 1 bar, to analyze the temperature dependence of λ_{quantum} [46],

$$\lambda_{\text{quantum}} \sim T^\chi, \quad (9)$$

we estimated the power χ by the least squares fitting. It yielded

$$\begin{aligned} \chi &= -0.28, \text{ for LQDL at 1 bar,} \\ \chi &= -0.58, \text{ for HQDL at 1 bar.} \end{aligned} \quad (10)$$

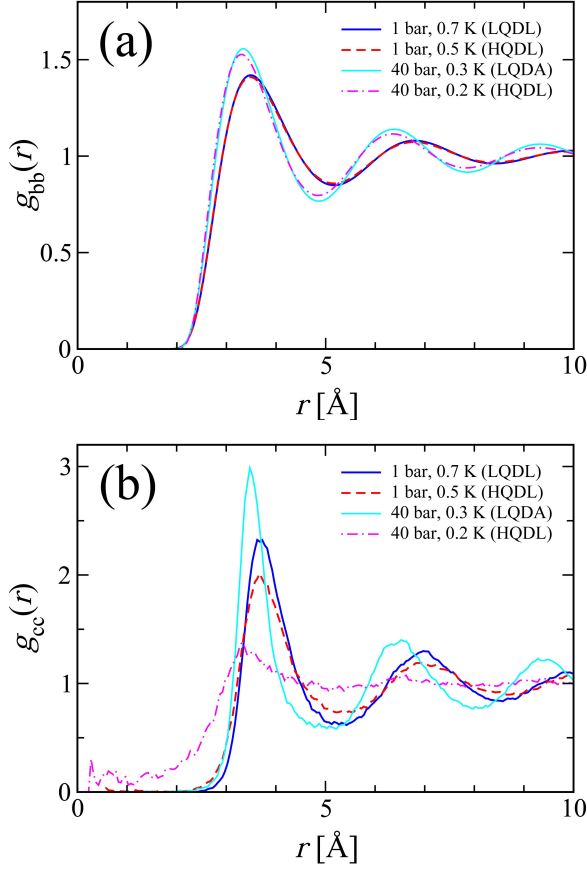


FIG. 6. The radial distribution functions at selected P - T conditions. (a) bead-bead radial distribution function g_{bb} ; (b) centroid-centroid radial distribution function g_{cc} . The g_{bb} is observable by diffraction experiments, whereas the g_{cc} is unobservable because atoms do not exist at centroid positions.

Surprisingly, these values are nearly equal to those of the two detailed states of supercritical fluid (SCF) ^4He ($-0.29 \leq \chi \leq -0.26$ for liquid or liquid-like state, $-0.49 \leq \chi \leq -0.46$ for the gas or gas-like state).[46] In this sense, the LQD-HQD boundary in the λ - T plot is similar to the Widom line [46] that separates the liquid-like and gas-like SCF states by the C_P maxima. However, as seen in Sec. IIIB, there are no traces of such C_P maxima in the present case.

The state transition can be detected more clearly by use of expansion factor $\alpha := \lambda_{\text{quantum}}/\lambda_{\text{quantum}}^{(0)}$ where the denominator is the quantum wavelength of a three-dimensional free particle, $\lambda_{\text{quantum}}^{(0)} = (h/2)\sqrt{3\beta/m} = \sqrt{3/8\pi}\lambda_{\text{dB}}$ [21]. We can regard α as being equivalent to expansion factor in polymer physics, i.e., $\alpha \approx R_g/R_g^{(\text{free})}$, where $R_g^{(\text{free})}$ is the radius of gyration of classical free ring polymer. Figure 8(a) shows the temperature dependence of α . In every isobar there exists a minimum or the tipping point locating at 0.2-0.6 K. As the temperature lowers, α decreases in the LQDL and

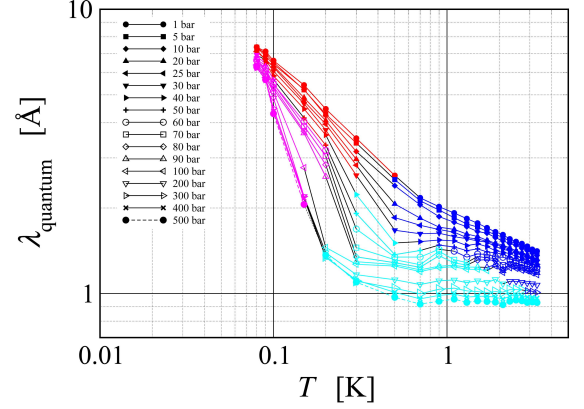


FIG. 7. A double logarithm plot of the quantum wavelength vs temperature. The colors of the symbols are the same as those displayed in Fig. 1: LQDL (blue), LQDA (cyan), HQDL (red), and HQDA (magenta).

LQDA, whereas it reversely increases in the HQDL and HQDA. Namely, each minimum point in this α - T plot is the transition point between an LQD state and an HQD state. A positive (negative) slope of the α - T curve corresponds to an LQD state (an HQD state), respectively.

Figure 8(b) shows the replot of α shown in Fig. 8(a) as a function of quantumness parameter Λ^* . Here the interatomic closest distance σ was taken as the distance of the first peak of g_{bb} . In this figure, Λ^* of the HQD states are higher than those at tipping points. Interestingly, the Λ^* at the tipping points ($1 \lesssim \Lambda^* \lesssim 3$) is in good agreement with Λ^* in the quantum binary Lennard-Jones system ($1 \lesssim \Lambda^* \lesssim 2$) [8, 9]. Seemingly, in Fig. 8(b), plotted points of LQD states tend to gather on a single curve which is possibly located at yellow background region. This suggests the universality of the relation between α and Λ^* of the LQD states, whereas the data points of the HQD states are remarkably deviated from it.

We comment on the bead number dependence of λ_{quantum} and α . The examination of this dependence was examined by short CMD runs at 1 bar, and the graphs are shown in Fig. SA-3 in the Supplementary Material. In Fig. SA-3(a), clearly, remarkable increase of λ_{quantum} with lowering temperature toward 0.1 K is observed for every N_b . Further, in Fig. SA-3(b) the reentrant temperature-dependence of α passing the tipping points is recognized for all N_b conditions. Therefore, the occurrence of the LQD-HQD transition is essential and is not an artifact.

E. Apparent self-diffusion coefficient

In Figs. SB-3 and SB-4 in the Supplementary Material, we provide the mean square displacement (MSD) of

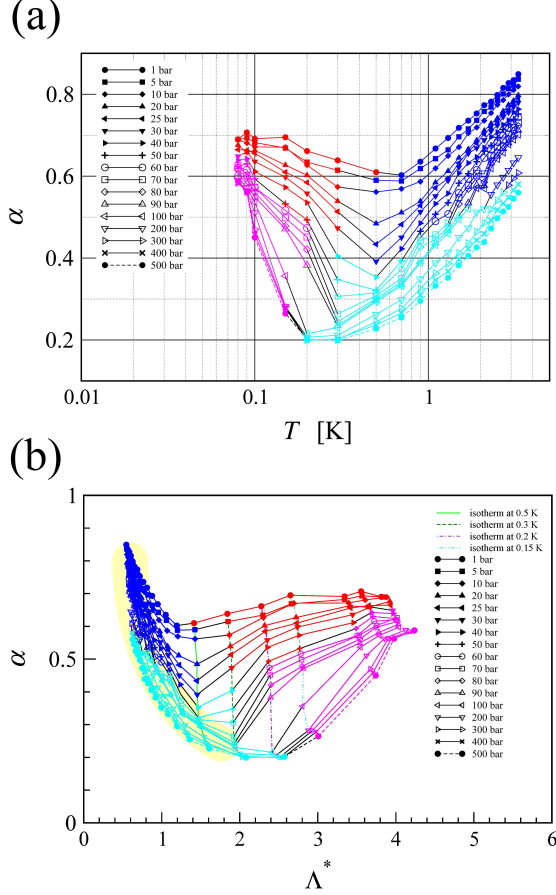


FIG. 8. The expansion factor vs (a) temperature and (b) quantumness parameter. The colors of the symbols are the same as those displayed in Fig. 1: LQDL (blue), LQDA (cyan), HQDL (red), and HQDA (magenta). In (b), when there is a relation between the de Broglie thermal wavelength and the closest distance, $\lambda_{dB} \geq \sigma$, we get $\Lambda^* \geq 1/\sqrt{2\pi} = 0.40$. The yellow background shown in (b) denotes a possible universal curve for the LQD states.

atomic centroids,

$$R^2(t) = \frac{1}{N} \sum_{i=1}^N \langle |\mathbf{r}_{ci}(t+t_0) - \mathbf{r}_{ci}(t_0)|^2 \rangle_{t_0}. \quad (11)$$

The Einstein relation, $R^2(t) = 6Dt$ ($t \rightarrow \infty$), holds when atoms diffuse according to Brownian motion characteristic of liquid phase. However, in the present study, apparent self-diffusion coefficient D was conveniently estimated by fitting the $R^2(t)$ to this linear relation over $0 \leq t \leq 4$ ps. Therefore, such an estimated D is not a true self-diffusion coefficient but an apparent value merely reflecting the speed of atomic displacement. When we get $R^2(t=4\text{ ps}) \leq 0.5 \text{ \AA}^2$, i.e., $D \leq 2 \times 10^{-6} \text{ cm}^2\text{s}^{-1}$, the system was regarded as being solidified, otherwise being in a liquid state; the existence of gas phase was denied from the molar volume (Fig. 3). Since there is no indication of

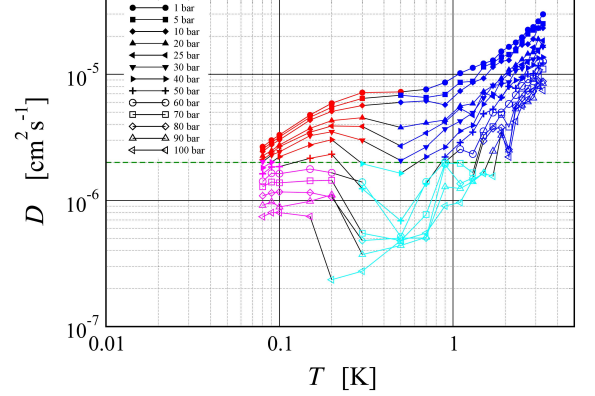


FIG. 9. The temperature dependence of apparent self-diffusion coefficient below 100 bar. The colors of the symbols are the same as those displayed in Fig. 1: LQDL (blue), LQDA (cyan), HQDL (red), and HQDA (magenta). Green horizontal dashed line denotes the threshold between liquids and glasses ($D = 2 \times 10^{-6} \text{ cm}^2\text{s}^{-1}$).

crystalline structure as described in Sec. III C, the solidification in the present work means the glassification. The temperature dependence of D is shown in Fig. 9 ($P \leq 100$ bar) and Fig. SA-13 ($P \geq 200$ bar) in the Supplementary Material. In Fig. 9, there is a tendency that D decreases with lowering temperature in LQDL and LQDA. However, as for the isobars at $P \geq 20$ bar, further drop of T causes D to turn to increasing on the occasion of the LQD \rightarrow HQD transition, and the increase is more drastic at higher pressures. The increase of D occurring at the LQDA \rightarrow HQDA transition for $P \geq 60$ bar indicates the reentrant behavior that the residual diffusion is enhanced by the glass-glass transition; this tendency agrees with the previous observation of the pressure or temperature-induced reentrant tendency of D [8, 9, 21]. However, we note that the liquid-liquid transition from LQDL to HQDL also increases D at $20 \leq P \leq 30$ bar, indicating the reentrant behavior, though this is not recognized at lower pressures, $1 \leq P \leq 10$ bar. We also find that the temperature lowering of LQDA at 40 and 50 bars leads to melting into the HQDL state (*melting by cooling*).

Finally, we provide the D - Λ^* relation in Fig. SA-14 in the Supplementary Material. Compared with Fig. 9, the plotted points of LQD states seemingly tend to be located on a single line. This suggests the possible universality of the D - Λ^* relation underlying the LQD states.

F. Identification of states

On the basis of the results presented in Secs. IIIB-III E, we identified the state at each P - T point by following the criteria (1)-(3):

- (1) When there is non-zero distribution of g_{cc} at r

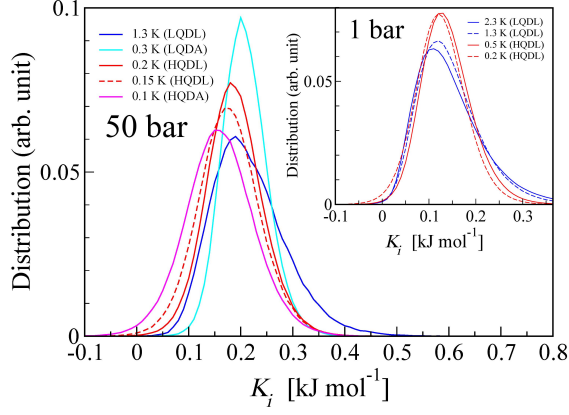


FIG. 10. The probability distributions of contributing term K_i at 50 bar and 1 bar. The main graph and the inset show the distributions at 50 bar and 1 bar, respectively. The colors of the curves are the same as those displayed in Fig. 1: LQDL (blue), LQDA (cyan), HQDL (red), and HQDA (magenta).

shorter than the closest distance observed in g_{bb} , this evidences the HQD state, otherwise the state is classified into the LQD state (Sec. IIIC)

(2) The increasing and decreasing α with isobaric lowering of temperature corresponds to HQD and LQD state, respectively (Sec. IIID).

(3) The apparent self-diffusion coefficient $D \geq 2 \times 10^{-6} \text{ cm}^2 \text{ s}^{-1}$ corresponds to a liquid state, otherwise the state is regarded as a glassy solid (Sec. IIIE). There are no crystal states (Sec. IIIC).

The conclusion of such identification of the system state was summarized in Fig. 1. Here, after plotting the identified points on the P - T plane, the boundary lines were drawn passing between two adjacent points representing the two different states. In this figure, we discarded the data points at $T < 0.1$ K from the plot because we cannot deny possible artifact due to the insufficiency of the number of beads ($N_b = 500$) at these lowermost temperatures.

G. Quantum tunneling of atoms

Figure 10 shows the probability distributions of contributing term K_i (Eq. (6)). As we showed in our previous paper [21], negative K_i denotes the existence of tunneling atoms whose necklaces bestride on saddle points of the potential surface. We can see no negative K_i for all the presented conditions in the LQD states. There is only a small portion of non-zero distribution of negative K_i in the HQD states, in particular, at lowermost temperatures. This indicates that atomic tunneling is rare even in HQD states. The distribution of negative K_i we see here is much less than that in compressed HQDA [21] where the atomic tunneling occurs as a consequence

of the explosive expansion of necklaces induced by far higher pressure. Therefore, we can conclude that ^4He atoms diffuse in each of HQDL and LQDL with *almost* no quantum tunneling, while this is in contrast to the highly compressed HQDA where the residual diffusion is enhanced by the tunneling effect [21].

Among the graphs at 50 bar, the HQDA at 0.1 K and 50 bar has the largest population of negative K_i . This seems to be in harmony with the double-well tunneling model to explain the linear temperature-dependence of heat capacity, $C_V \sim T$, of quantum glasses near $T \sim 0$ [10, 11]. The existence of a low concentration of tunneling atoms in HQDL at lowermost temperatures likely suggests a possible deviation from the heat capacity in the phonon regime, $C_V \sim T^3$, in this liquid state near $T \sim 0$ if it exists.

H. Centroid velocity autocorrelation function

Figure 11 shows the centroid velocity autocorrelation function (VAF) at the P - T points on the both sides of each HQDL-LQDL and HQDL-LQDA boundary. Clearly, the VAFs of the LQDL exhibit an oscillatory decay characteristic of liquid state, whereas the decay in HQDL is rather monotonous or damped oscillatory. This distinction is similar to the clearer dynamic crossover at the Frenkel line in the SCFs [56]. For SCFs above the Frenkel line the VAF exhibits a monotonous decay and the state is identified as a gas-like SCF, while below the line it exhibits an oscillatory decay by which the state is regarded as a liquid-like SCF [46, 56].

For example, in Fig. 11(b), in the occasion of the HQDL-LQDA isobaric transition ($0.2 \leftrightarrow 0.3$ K) at 40-50 bar, the VAF changes its profile as if the Frenkel line is crossed over. Therefore, from the VAF point of view, we can say that the HQD-LQD boundary line is akin to the Frenkel line. However, HQDL is neither gas nor gas-like SCF because molar volume is not so much expanded (Fig. 3). The gentle relaxation in HQDL is a consequence of atomic dynamics driven by mild centroid force \mathbf{F}_{ci} (Eq. (5)), i.e., the remarkably weak interatomic force smoothed out by stretched necklace configurations. Thus, the atoms in HQDL diffuse without remarkable oscillation and noticeable tunneling (Sec. IIIG). Further analysis of dynamical properties of this novel liquid is to be reported in our next paper.

IV. ANALYSIS BASED ON THE STATE DIAGRAM

In this section, we analyze the state diagram shown in Fig. 1, referring to the physical properties provided in the last section.

First, we find that at $P \leq 25$ bar the present system does not freeze down to 0.08 K. This indicates the ease of melting of the present Boltzmann system at low T

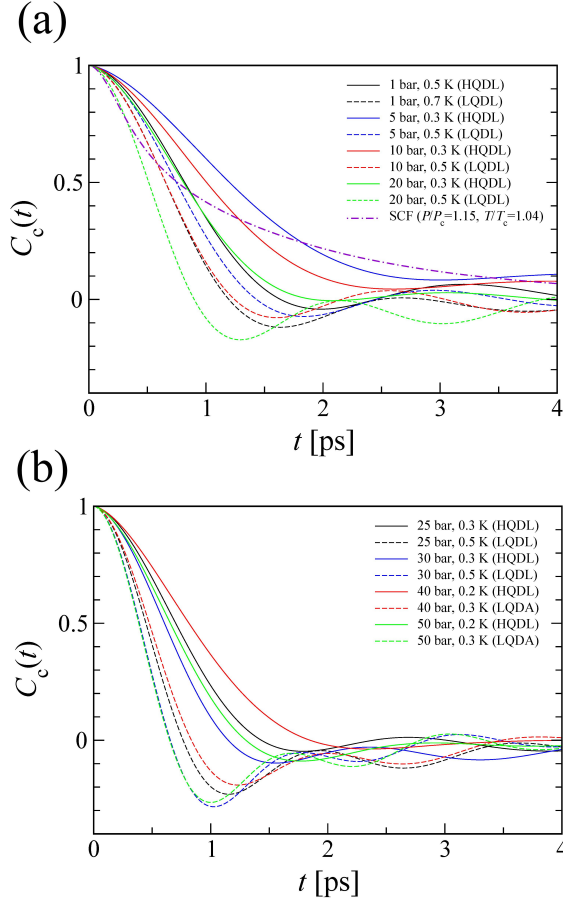


FIG. 11. The centroid velocity autocorrelation functions at the neighboring P - T points on the both sides of the HQD-LQD boundary. (a) $P = 1 - 20$ bar; (b) $P = 25 - 50$ bar. Solid lines: HQDL; dashed lines: LQDL or LQDA. The two points of both sides at the same pressure are drawn in the same color. For comparison, in (a) we also plot the curve for the supercritical fluid state (SCF) at $P/P_c = 1.15$ and $T/T_c = 1.04$ (P_c and T_c is critical pressure and temperature, respectively) [46].

and low P even though there is not Bosonic permutation effect leading to the emergence of BEC. The NQE solely caused the liquid state to persist down to 0.08 K in this pressure range.

We presumed that the melting line was located at somewhat lower pressures than the glass transition line. This is because the overpressurization should be caused by unavoidable hysteresis due to unrealistically rapid compression in computer simulation. In addition, for real ^4He , the ease of overpressurization inherent in this substance was experimentally reported [57, 58]. The obtained glass transition line in Fig. 1 is not the ideal glass transition line (the Kauzmann curve) [36, 37].

In Fig. 1, the presumed melting curve drawn in parallel with the glass transition line is downward convex and has a minimum at $T_{\min} \cong 0.4$ K and $P_{\min} \cong 25$ bar. In gen-

eral, a melting line with an extremum can be related to the occurrence of liquid polyamorphism [35]; two liquid states may exist at higher and lower temperatures than T_{\min} . In accordance with this, the LQDL-HQDL boundary line emanates from the vicinity of the minimum of the presumed melting curve. This boundary line is located in parallel with the experimental λ transition line, and is shifted low by about 1.8 K. Boninsegni et al. presumed the phase diagram of distinguishable ^4He , where the solid-liquid boundary was also downward convex [5]. In fact, the experimental melting curve of ^4He (^3He) has a shallow minimum at $T_{\min} = 0.8$ K and $P_{\min} = 26$ bar for ^4He (0.3 K and 29 bar for ^3He). The melting line in Fig. 1 is much more emphasized convex than the real system.

When a state point on the P - T plane moves across the HQDL-LQDA boundary line within the range of $0.2 \leq T \leq 0.3$ K and $40 \leq P \leq 50$ bar, *melting by cooling* (*freezing by heating*) or exothermic melting (endothermic freezing) occurs; these transitions are alternatively called inverse melting (freezing) [36–41, 59]. Thus, the state diagram evidences the occurrence of isobaric inverse melting (freezing). In order to confirm it, however, such inverse freezing of HQDL by heating was examined in this study, and the results are shown in Appendix A; we succeeded in observing the inverse freezing in this test simulation.

In Fig. 3, we can see that there is a temperature range with negative slopes of the V - T line at $20 \leq P \leq 90$ bar. This indicates negative isobaric thermal expansion,

$$\alpha_P = \frac{1}{V} \left(\frac{\partial V}{\partial T} \right)_P = -\frac{1}{V} \left(\frac{\partial S}{\partial P} \right)_T < 0. \quad (12)$$

Therefore, entropy increases by the isothermal compression from LQDL to LQDA. The negative thermal expansion is also true for real solid ^4He [60, 61].

The Clausius-Clapeyron equation denoting the slope of melting line is expressed as

$$\frac{dP_m(T)}{dT} = \frac{\Delta S_{1 \rightarrow 2}}{\Delta V_{1 \rightarrow 2}} = \frac{\Delta H_{1 \rightarrow 2}}{T_m \Delta V_{1 \rightarrow 2}}, \quad (13)$$

where $\Delta X_{1 \rightarrow 2} := X_2 - X_1$ is the change of X in the process from state 1 to 2 at the melting temperature T_m . At the minimum of melting curve (P_{\min}, T_{\min}), we get $\Delta S = 0$, indicating that the entropy of solid and liquid is equal. Therefore, we regard this point as the Kauzmann point at which the melting curve and the ideal glass transition line, yet unrevealed, cross with each other [36, 37].

We further proceed analysis of the results by rereading Eq. (13) as a pseudo-Clapeyron equation which approximately holds for the slope of glass transition line [62],

$$\frac{dP_m(T)}{dT} \cong \frac{dP_g(T)}{dT} \cong \frac{\Delta H_{1 \rightarrow 2}}{T_g \Delta V_{1 \rightarrow 2}}, \quad (14)$$

where P_g and T_g are the glass transition pressure and temperature, respectively, while $\Delta V_{1 \rightarrow 2}$ and $\Delta H_{1 \rightarrow 2}$ are

the volume and enthalpy change over a finite temperature width $\Delta T_{1 \rightarrow 2}$ riding on the glass transition line, $T_1 < T_g < T_2$, respectively. As shown in Ref. 62, this approximated relation is never far from reality, because the difference between thermodynamic property X of a glass and the crystal is, in general, small enough and the slopes of the glass transition line and of the melting curve are nearly equal. A similar treatment was carried out in our previous study where the pseudo-Claapeyron equation was applied to the Widom line, which we regarded as the pseudo-boiling line separating the gas-like and liquid-like SCF [46]. In Fig. 3, we can see $\Delta V = V_{\text{LQDA},0.3\text{K}} - V_{\text{HQDL},0.2\text{K}} < 0$ at $0.2 \leq T_g \leq 0.3$ K for the isobars of 40 and 50 bars, while in Fig. 4 enthalpy change with increasing T is always positive, $\Delta H > 0$, for any isobars. Accordingly, Eq. (14) yields $dP_m/dT \cong dP_g/dT < 0$, coinciding with negative slope of the left half ($T < T_{\min}$) of the glass transition line and presumed melting line in Fig. 1. Therefore, the presumed equilibrium crystal phase overlapping on the convex region of LQDA at 0.3 K and 40-50 bars should have larger entropy than the HQDL at 0.2 K and 40-50 bars. On the other hand, the slope of the right half ($T > T_{\min}$) of the glass transition line and the presumed melting line are positive, $dP_m/dT \cong dP_g/dT > 0$, indicating the normal melting (melting by heating). This is because we can see, in the range of $0.4 \leq T \leq 3.3$ K and $40 \leq P \leq 500$ bar, $\Delta H_{\text{solid(LQDA)} \rightarrow \text{liquid(LQDL)}} > 0$ (Fig. 4) and $\Delta V_{\text{solid(LQDA)} \rightarrow \text{liquid(LQDL)}} > 0$ (Fig. 3). Thus, the analysis based on the pseudo-Claapeyron equation evidences the downward convex curves of the glass transition line and the presumed melting line shown in Fig. 1.

As described in Sec. I, the present system should be liquid at $T = 0$. Since this should not violate the third law of thermodynamics, the system must be in a single state without degeneration [6, 63]. At $T = 0$, therefore, the liquid phase must have zero entropy equal to the crystal phase existing at higher pressures, so that the presumed melting line should be horizontal owing to the Clausius-Claapeyron equation, Eq. (13). Although this line was drawn down to 0.1 K in Fig. 1, at present, it is unknown whether this becomes horizontal even at non-zero temperatures such as 0.01 or 0.001 K before reaching $T = 0$. This issue would be revealed in a future work, together with exploring the possibility of another liquid polymorph at such lower temperatures.

Figure 12 shows the extended state diagram which includes the data points at $3 \leq T \leq 25$ K provided in our previous paper [21]. Since the LQDL covers the P - T conditions of He-I of real ^4He , this state is considered as being nearly identical to He-I. Indeed, in our previous works, we showed that the properties of He-I were well reproduced by the CMD simulations obeying Boltzmann statistics [21, 46, 64]. However, LQDL is not completely identical to He-I because it does not involve Bosonic permutation effect though it must be negligibly weak in He-I [46]. In this figure, we can see that the HQD states, in general, exist at higher P and lower T , i.e., at higher

quantumness condition than LQD states.

Finally, it should be noted that any state diagram including metastable states is apt to depend considerably on the production process in the simulations, as we saw in our previous work [21]. The production history, time increment [21], and adopted algorithm would affect the emergence of states. Therefore, we should consider that the state diagrams, Figs. 1 and 12, are not absolutely definitive and another production procedure would possibly yield a modified state diagram.

V. DISCUSSIONS

A. On state transition

As shown in Sec. IIIB, there is no discontinuity in the H - T plot and no maximum in the C_P - T relation even when the LQD-HQD state transitions occur. This denies that the LQD-HQD transitions are the first- or second-order phase transitions and supports that they are continuous crossovers. This is in contrast to the fact that the ideal Bose gas exhibits a cusp at the BEC temperature T_C in the C_V - T plot [6] and that even the ideal quantum Boltzmann gas possesses a peak as well [65]. For ideal Bose gas, as the number of atoms decreases from the thermodynamic limit ($N \rightarrow \infty$), the cusp of the C_V - T plot becomes smeared-out [66]. This indicates a finite-size effect; in the C_P - T relation of the confined ^4He , not the λ -like peak but the blunted shape emerges [67–69]. However, the lack of maximum in the C_P - T plot in this study is not because of the size effect. Although the number of atoms in the present simulations is finite ($N = 256$), the periodic boundary condition ensures to reproduce the bulk properties [21, 46, 64]. Therefore, the smooth change of H and V with varying temperature in the LQDL-HQDL transition is considered as being a bulk property. This indicates that this transition is continuous crossover, not the thermodynamic transition.

In Sec. IIID, the analysis of temperature dependence of quantum wavelength λ_{quantum} showed the change of the power χ in Eq. (9) on the occasion of LQDL-HQDL transition at 1 bar. The change of χ also happens when the state point crosses over the Widom line in the SCF state of ^4He . However, there is no appearance of the C_P maximum on the LQDL-HQDL transition (Sec. IIIB). On the other hand, also at the LQDL-HQDL transition, the VAF exhibits the profile change which is similar to that on the Frenkel line of the ^4He SCF (Sec. IIH). Originally, this line is not a thermodynamic boundary but a dynamic boundary. The present LQDL-HQDL boundary is not the thermodynamic boundary because of the lack of C_P maximum. In this sense, it is closer to the Frenkel line. However, we again note that both LQDL and HQDL are not SCF but liquid states without expanded volume.

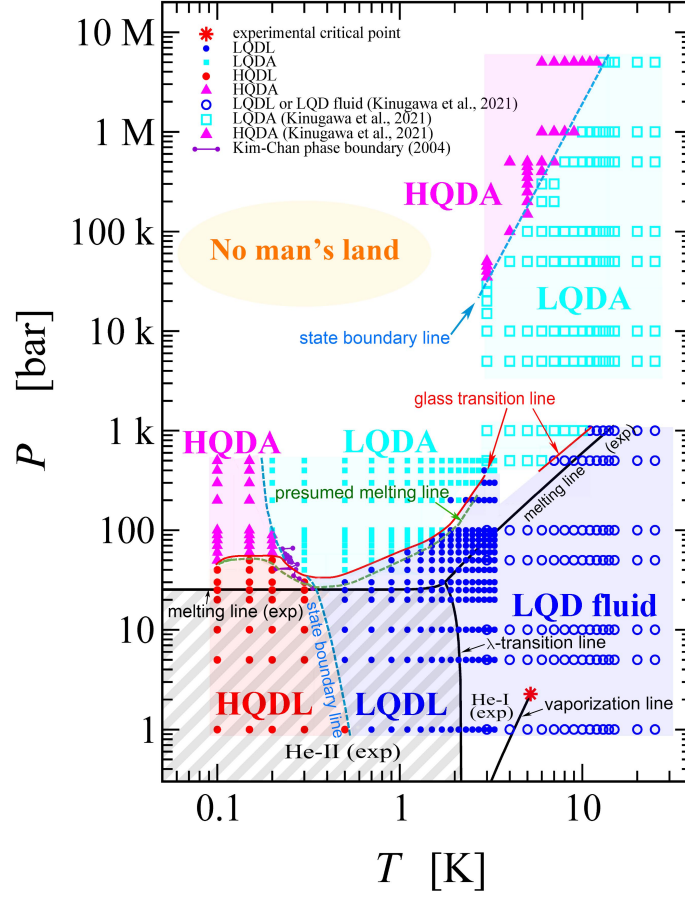


FIG. 12. The state diagram of distinguishable ^4He obtained from isothermal compression over wider P - T range. LQDL (blue): low quantum dispersion liquid; HQDL (red): high quantum dispersion liquid; LQDA (cyan): low quantum dispersion amorphous solid (metastable); HQDA (magenta): high quantum dispersion amorphous solid (metastable). “LQD fluid” includes LQDL, gas (in LQD state), and supercritical fluid (in LQD state) existing beyond the critical point (red star). Black solid lines are the experimental phase boundary lines of real ^4He . Experimentally, He-I and He-II (gray slant stripe) exist at higher and lower temperatures than λ transition line (black), respectively, while the crystalline solid phase exists at pressures higher than the melting curve (black). The open symbols are the points explored by the isothermal compression simulation in our previous study [21]. The Kim-Chan boundary line is cited from Ref. 32.

B. State metastability and statistical mechanical effect

In Fig. 5, we can see that the data points of He-I, He-II, and solid phase of real ^4He lie on a universal line. This line, in other words, denotes the K - V relation which corresponds to the global minimum of the free energy, since He-I, He-II, and solids phase are all at thermodynamic equilibrium. However, the points of HQDL are extensively scattered on the plane and are downward deviated from the universal line. Therefore, if we introduced the Bosonic permutation to the present system, these deviated points of HQDL would be metastable points. This means that the HQDL can exist only as a metastable

state (if it can exist), not as an equilibrium state in reality (i.e., in the regime of Bose statistics).

However, we would mention that, plausibly, HQDL is metastable even in Boltzmann statistics. One main reason is that the HQDL-LQDL transition by varying temperature is continuous without any indication of thermodynamic transition. The LQDL-to-HQDL transition by isobaric cooling should be similar to a glass transition in that a metastable state is formed from an equilibrium state without discontinuous change of enthalpy. Both transitions should depend on the production process and hysteresis. The second reason is, being intuitive, that the wide scatter of K - V points of HQDL seemingly reflects the ease of emergence of many configurations of stretched

flexible necklaces. This can be plausible because the springs of atomic necklaces are remarkably loosed by low temperatures. There should be many local free-energy minima corresponding to necklace configurations in such stretched flexible *polymer* system.

In fact, we examined another CMD simulation of isothermal decompression of the crystal of distinguishable ^4He for 0.1-0.9 K, starting from 100 bar (the pressure at experimental solid phase region) [70]. Even down to 1 bar, the crystal state persisted at the P - T conditions where the LQDL or HQDL were produced in the main simulation of this study. We obtained, for example, the enthalpy at 0.5 K and 1 bar, $H = -0.057 \pm 0.004 \text{ kJmol}^{-1}$ for HQDL and $-0.058 \pm 0.004 \text{ kJmol}^{-1}$ for the crystal. Namely, the enthalpy difference is negligible within the standard deviation. Therefore, we cannot say that the crystal is energetically stabler than HQDL. Rather, this crystal state should be regarded as being as metastable as HQDL. Accordingly, both HQDL and the crystal obtained from the decompression must be metastable states under Boltzmann statistics. Every state produced in the experimental He-II region by the Boltzmann-type simulations should plausibly be metastable and correspond to each local free-energy minimum. As a result, during the simulations each state was allowed to exist quasi-stably as it was. If we introduced Bose statistics to this system, these local minima would be converged into a global free-energy minimum, which corresponds to the true thermodynamic equilibrium state, He-II. This should be akin to the gelation of sol, which is equivalent to the emergence of BEC by polymerizing the necklaces [71]. It seems to be difficult to judge which metastable state is the stablest and at the thermodynamic equilibrium in the Boltzmann regime, because energetic difference is quite negligible and estimation of entropy is burdensome. Further examination of the metastability would be a future subject. Regardless of the discussion of metastability, it is important that one metastable state called HQDL below 25 bar succeeded in non-freezing down to 0.1 K in the present investigation.

As in our isothermal decompression test, the retention of crystal state at 0.5 K and $24.3 \text{ cm}^3\text{mol}^{-1}$ was reported for distinguishable ^4He [5]. This can also be attributed to the above-mentioned metastability of each state in distinguishable ^4He . The retention of the crystalline states, observed in our and their simulations, seems to be non-trivial, considering that distinguishable ^4He should be liquid at $T = 0$ as described in Sec. I. However, simple extrapolation from the zero-temperature limit does not predict what state or liquid polymorph emerges at a given P - T point for $T > 0$.

The flexibility of necklaces and metastability of each state points endorse high *fragility* [14, 37] of this liquid state. Because of metastability of HQDL, it is probable that another production procedure makes the state boundary lines shown in Fig. 1 be shifted on the P - T plane. It is also probable that the properties shown in Sec. III are somewhat deviated from the present.

One also sees in Fig. 5 that the K of the HQD states is lower than the experimental universal line. This suggests that atomic necklaces of HQD are more stretched than even He-II. This can be attributed to the lack of the Bosonic correlation. In fact, introducing the Bosonic permutation effectively corresponds to the addition of attractive correlation to the system [6]. It is known that this makes a VAF be more oscillatory than that in the Boltzmann regime [72]. Therefore, the VAF of HQDL shown in Fig. 11 should be less oscillatory than the real He-II obeying Bose statistics. On the other hand, seemingly, the lower kinetic energy of HQDL than LQDL is in accordance with more gas-like diffusion.

It is anticipated that the off-diagonal density matrix $\rho(r)(= \rho(|\mathbf{r} - \mathbf{r}'|))$, i.e., the end-to-end distribution of isomorphic open chain polymer, may possess a non-zero distribution at $r \lesssim \lambda_{\text{quantum}}$. The momentum distribution function $\tilde{\rho}(k)$, i.e., the Fourier transform of $\rho(r)$, should then possess a sharp distribution at $k \sim 0$. This is the situation close to the BEC where $\tilde{\rho}(k)$ has an infinite peak at $k = 0$ (momentum degeneration). Although we did not evaluate $\rho(r)$ in this study, long λ_{quantum} in HQD states is considered as a precursor of the BEC, prior to beginning the polymerization by introducing the atomic permutation. Such polymerized open chains would exhibit even longer end-to-end distribution in $\rho(r)$ [73].

In Appendix B, we compared the present state diagram with the experimental results of confined sub-nano scale systems and *supersolid* of real ^4He .

VI. CONCLUSIONS

In the present study, the path integral CMD simulation for distinguishable ^4He obeying Boltzmann statistics was conducted in the range of $0.08 \leq T \leq 3.3 \text{ K}$ and $1 \leq P \leq 500 \text{ bar}$. The P - T thermodynamic conditions were strictly controlled by means of the isothermal-isobaric CMD method to provide computational results with high quantitateness. On the basis of the isothermal compression simulations, we revealed the state diagram of this ideal model system on a P - T plane ($0.1 \leq T \leq 3.3 \text{ K}$ and $1 \leq P \leq 500 \text{ bar}$). The conclusions are summarized as follows:

(1) Even though this system does not include the Bosonic permutation effect, it does not freeze down to 0.08 K when the pressure is below 25 bar. The non-freezing property of ^4He is fulfilled by sole NQE, not needing to introduce Bose statistics.

(2) There can exist two liquid states in distinguishable ^4He . One liquid state is LQDL which is nearly identical to normal liquid He-I. The other is HQDL, which consists of atoms with wider spatial extension of necklaces and exists at lower temperatures ($T \leq 0.5 \text{ K}$) than LQDL. There can be two glass states, LQDA and HQDA, corresponding to the two liquid states, and they were the same as those discovered at higher temperatures and pressures in our previous work. These glass states are considered

as metastable states which should eventually become the crystal phase as the thermodynamic equilibrium state.

(3) The HQDL is a non-superfluid state with lower entropy than the solid (LQDA) existing at higher temperatures. It can exist only as a metastable state under Bose statistics (if it exists). Plausibly, it is also metastable even in the Boltzmann regime. The HQDL is a *fragile* liquid involving many configurations of stretched flexible necklaces. This fragility benefits the occurrence of liquid polyamorphism in distinguishable ^4He . The velocity autocorrelation function of HQDL exhibits such a relaxation as observed in the gas-like supercritical fluid above the Frenkel line. In HQDL, the atoms diffuse without noticeable contribution from quantum tunneling.

(4) The presumed melting line on the P - T plane is downward convex and has a minimum point at $T \simeq 0.4$ K and $P \simeq 25$ bar, from which the LQDL-HQDL boundary line emanates, as an indication of liquid polyamorphism. Since there is no C_P maximum at this transition, the LQDL-HQDL transition is not a thermodynamic phase transition but a continuous crossover. Observable structural change by the transition is smooth and continuous. Thus, the existence of these two liquids is not conventional classical polyamorphism but the *quantum polyamorphism* characterized by the change of atomic quantum dispersion. The temperature dependence of quantum wavelength and of its expansion factor remarkably changes on the occasion of the LQDL-HQDL transition.

(5) At 40-50 bar, the HQDL undergoes the inverse freezing (endothermic *freezing by heating*) into LQDA when it is heated from 0.2 K to 0.3 K. This inverse freezing is accompanied with the change of spatial extension of atomic necklaces. This resembles the coil-globule transition in classical polymer systems.

(6) There are only negligible portions of tunneling atoms in all the states: HQDL, LQDL, HQDA, and LQDA.

Finally, in Appendix B, the state diagram of this study was compared with the experimental reports of confined systems and *supersolid* of real ^4He . A part of P - T region of HQDL overlaps with that of the real non-superfluid states (the LBEC and the BEC-like low-entropy state) of ^4He confined in nanopores in meso-porous materials, which should be more Boltzmann-like (or suppressed Bosonic) than the bulk. Further, the P - T region of the HQDL causing inverse freezing almost overlaps with the reported *supersolid* region neighboring to the Kim-Chan state boundary. These comparisons provide a future subject as to a question whether HQDL has some essential relevance to these real systems.

This is the first investigation that revealed the state diagram, the existence of liquid polyamorphism, and inverse freezing in distinguishable ^4He without inclusion of Bosonic statistical effect. As a future subject, it is intriguing to investigate whether the sole NQE would generate another liquid polymorph when the system is

cooled down to far lower temperatures such as 1 mK before reaching $T = 0$, at which distinguishable ^4He should be a liquid. It is also unrevealed whether even more “classical” systems such as Ne and Ar can melt at extremely low temperatures solely by the NQE when the temperature is extremely lowered. The universality of quantum liquid polyamorphism induced by NQE is still an open question.

Appendix A: TEST OF FREEZING BY HEATING

In Appendix A, we provide the results of another CMD simulation to test the inverse freezing. In Fig. 1, we can see that an isobaric heating of the HQDL at 40 bar, starting from 0.2 K toward 0.3 K, may induce solidification or inverse freezing (*freezing by heating*). To check this, starting from the end configuration of the production run at 0.2 K and 40 bar, we conducted three isobaric CMD runs. One of them was carried out keeping the temperature at 0.2 K, while the other runs were the process of raising the set temperature to 0.3 or to 0.4 K.

The results of the MD time evolution of λ_{quantum} are shown in Fig. 13. In this figure, λ_{quantum} retains about 3.5 Å when the temperature is kept at 0.2 K. In contrast, it starts to be shortened right after the temperature switching to 0.3 or 0.4 K at $t_{\text{MD}} = 5$ ps. The quantum wavelength finally resulted in $\lambda_{\text{quantum}} = 1.7 - 1.8$ Å, which is even shorter than 2.2 Å at 0.3 K (LQDA) shown in Fig. 7.

The g_{cc} before and after heating are shown in Fig. 14, while the MSDs for the states before and after the temperature switching are shown in the inset. The non-zero distribution characteristic of the g_{cc} of HQDL vanishes at 0.3 and 0.4 K. The apparent self-diffusion coefficient estimated from the MSD at 0.2 K and 40 bar is $D = 2.9 \times 10^{-6} \text{ cm}^2\text{s}^{-1}$, while D at 0.3 or 0.4 K is zero. Thus, judging from g_{cc} and D , we conclude that the transition from HQDL to LQDA, i.e., *glassification by heating*, occurred between 0.2 and 0.3 K. The transition process is visualized in Fig. SC-1 in the Supplementary Material, which shows the snapshot change with MD time. The final state attained at 0.3 K is a partially crystallized LQDA.

The average thermodynamic properties before and after the temperature switching are listed in Table SC-1 in the Supplementary Material. If we assume the HQDL→LQDA transition temperature as $T_{\text{tr}} = 0.25$ K, the pseudo-Claapeyron equation, Eq. (14), provides a negative slope of the transition line, $dP/dT = -1.14 \text{ kbarK}^{-1}$.

The increase of kinetic energy K in Table SC-1 in the Supplementary Material is explained by the shrinking of necklaces by the HQDL→LQDA transition. Since there is almost no concentration of negative K_i in the HQDL at 0.2 K before heating (Sec. III G), the HQDL→LQDA freezing transition is not a transition from tunneling to trapped regimes. This is unlike the situation occurring

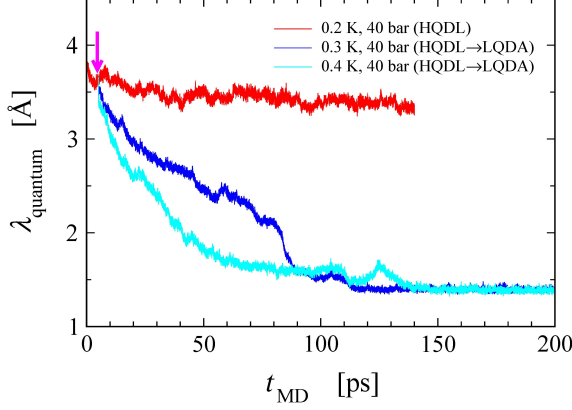


FIG. 13. The MD time evolution of quantum wavelength of ^4He atoms by isobaric heating test at 40 bar. The graphs show the results of three CMD runs with different control of temperature: (1) keeping the temperature at 0.2 K throughout the run; (2) raising temperature to 0.3 K at $t_{\text{MD}} = 5$ ps (pointed by a magenta arrow); (3) raising temperature to 0.4 K at $t_{\text{MD}} = 5$ ps (pointed by a magenta arrow).

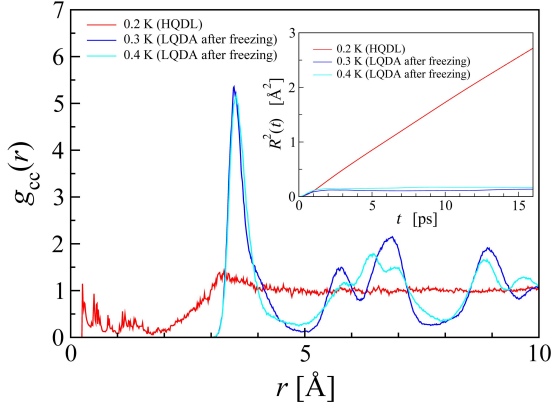


FIG. 14. The centroid-centroid radial distribution function g_{cc} and the mean square displacement $R^2(t)$ for the states before and after the isobaric heating test at 40 bar. The $R^2(t)$ is shown in the inset.

in compressed ^4He [21].

This test simulation showed that the inverse freezing (endothermic freezing) of HQDL was actually caused by isobaric heating from 0.2 to 0.3-0.4 K at 40 bar. This transition P - T agrees with the HQDL-LQDA boundary line drawn in the state diagram (Fig. 1). Thus, the present test yielded the same conclusion as we saw in Sec. IV. Although the P - T condition of the state boundary in Fig. 1 cannot completely be free from possible hysteresis of production process, the present agreement ensures that the HQDL existing in the upward convex region in Fig. 1 certainly freezes on the occasion of cross-

ing over the drawn HQDL-LQDA boundary line. This line almost overlaps with the Kim-Chan boundary, as described in Appendix B 2.

A similar type of inverse melting was observed for the classical systems such as water (the transition from low-density amorphous solid (LDA) to low-density amorphous liquid (LDL)) [16] and classical polymers [74, 75]. The higher entropy of the partially crystallized LQDA than HQDL can possibly be attributed to the existence of transverse phonon mode absent in liquid phase [36]. We note that the inverse freezing of this system is accompanied by the change of spatial extension of atomic necklaces, i.e., the atomic quantum dispersion. The structural change of individual necklaces resembles the coil-globule transition in classical polymer systems [23–31].

Appendix B: STATE DIAGRAM COMPARISON WITH NON-SUPERFLUID STATES OF REAL SYSTEMS

In Appendix B, withholding speculative interpretation, the present state diagram is compared with that of two types of real systems, (1) several confined ^4He systems and (2) reported *supersolid*.

1. Comparison with confined ^4He

Recent experiments targeting confined ^4He revealed that the non-superfluid states, unlike He-I and He-II, exist at temperatures lower than the λ -transition line of the bulk system [67, 76–85]. Under such confined conditions, the off-diagonal long-range Bosonic correlation is hindered by the wall of glass substrate pores, so that Bosonic permutation effect should partially be suppressed [76, 81]. Figure 15 shows the comparison of our state diagram with that of confined ^4He in three kinds of substrates. Shirahama and co-workers revealed that the localized BEC (LBEC) state of ^4He confined in Gelsil exists in the region between the boundaries of “ T_{B} , Gelsil” and “ T_{C} , Gelsil” [67, 76, 79–81]. For ^4He confined in the folded sheets meso-porous materials (FSM) (28 Å), Taniguchi et al. reported that the state at temperatures between “ T_{B} , FSM” and “ T_{C} , FSM” was not He-I nor He-II but a BEC-like state with low entropy [77]. In this figure, the experimental state boundaries have the same negative slopes as the HQDL-LQDA boundary line. Some part of the P - T regions of the LBEC and the low-entropy BEC-like states overlaps with the upward convex region ($18 \lesssim P \lesssim 35$ bar and $T \lesssim 0.35$ K) of the HQDL causing inverse freezing.

2. Comparison with reported supersolid ^4He region

In Figs. 1 and 15, the HQDL-LQDA boundary emanating from the point at $T = 0.3$ K and $P = 26$ bar traces

- [17] Y. Katayama, Y. Inamura, T. Mizutani, M. Yamakata, W. Utsumi, and O. Shimomura, *Science* **306**, 848 (2004).
- [18] M. A. Morales, C. Pierleoni, E. Schwegler, and D. M. Ceperley, *Proc. Natl. Acad. Sci. U. S. A.* **107**, 12799 (2010).
- [19] B. Nguyen, G. E. Lopez, and N. Giovambattista, *Phys. Chem. Chem. Phys.* **20**, 8210 (2018).
- [20] A. Eltareb, G. E. Lopez, and N. Giovambattista, *J. Chem. Phys.* **156**, 204502 (2022).
- [21] K. Kinugawa and A. Takemoto, *J. Chem. Phys.* **154**, 224503 (2021).
- [22] Here we should mention the abbreviation of these names. In Ref. 21, we abbreviated them as “LDA” and “HDA”, respectively. However, since these may be confused with the low and high density amorphous state of classical systems (e.g., water [15, 16]), we presently call them LQDA and HQDA instead.
- [23] I. M. Lifshitz, A. Y. Grosberg, and A. R. Khokhlov, *Rev. Mod. Phys.* **50**, 683 (1978).
- [24] C. Maffi, M. Baiesi, L. Casetti, F. Piazza, and P. D. L. Rios, *Nat. Commun.* **3**, 1065 (2012).
- [25] C. Wu and X. Wang, *Phys. Rev. Lett.* **80**, 4092 (1998).
- [26] M. Podewitz, Y. Wang, P. K. Quoika, J. R. Loeffler, M. Schauerperl, and K. R. Liedl, *J. Phys. Chem. B* **123**, 8838 (2019).
- [27] J. Ma, J. E. Straub, and E. I. Shakhnovich, *J. Chem. Phys.* **103**, 2615 (1995).
- [28] D. S. Simmons and I. C. Sanchez, *Macromolecules* **41**, 5885 (2008).
- [29] D. S. Simmons and I. C. Sanchez, *Macromolecules* **43**, 1571 (2010).
- [30] E. Sherman and G. Haran, *Proc. Natl. Acad. Sci. U. S. A.* **103**, 11539 (2006).
- [31] A. Matsuyama and F. Tanaka, *J. Chem. Phys.* **94**, 781 (1991).
- [32] E. Kim and M. H. W. Chan, *Science* **305**, 1941 (2004).
- [33] R. Hallock, *Phys. Today* **68**, 30 (2015).
- [34] J. Wilks, *An Introduction to Liquid Helium*, Oxford Library of the Physical Sciences (Clarendon, Oxford, UK, 1970).
- [35] E. Rapoport, *J. Chem. Phys.* **46**, 2891 (1967).
- [36] F. H. Stillinger, P. G. Debenedetti, and T. M. Truskett, *J. Phys. Chem. B* **105**, 11809 (2001).
- [37] F. H. Stillinger and P. G. Debenedetti, *Biophys. Chem.* **105**, 211 (2003).
- [38] M. R. Feeney, P. G. Debenedetti, and F. H. Stillinger, *J. Chem. Phys.* **119**, 4582 (2003).
- [39] N. Schupper and N. M. Shnerb, *Phys. Rev. E* **72**, 046107 (2005).
- [40] S. Prestipino, *Phys. Rev. E* **75**, 011107 (2007).
- [41] A. L. Greer, *Nature* **404**, 134 (2000).
- [42] L. D. Landau and E. M. Lifshitz, *Statistical Physics*, 3rd ed. (Pergamon, Oxford, UK, 1980) revised and enlarged by E. M. Lifshitz and L. P. Pitaevskii.
- [43] D. Chandler and P. G. Wolynes, *J. Chem. Phys.* **74**, 4078 (1981).
- [44] D. Frenkel and B. Smit, *Understanding Molecular Simulation: From Algorithm to Applications* (Academic Press, NY, 2002).
- [45] R. A. Aziz, A. R. Janzen, and M. R. Moldover, *Phys. Rev. Lett.* **74**, 1586 (1995).
- [46] A. Takemoto and K. Kinugawa, *J. Chem. Phys.* **149**, 204504 (2018).
- [47] G. J. Martyna, A. Hughes, and M. E. Tuckerman, *J. Chem. Phys.* **110**, 3275 (1999).
- [48] T. M. Yamamoto, *J. Chem. Phys.* **123**, 104101 (2005).
- [49] K. R. Glaesemann and L. E. Fried, *J. Chem. Phys.* **117**, 3020 (2002).
- [50] M. E. Tuckerman, B. J. Berne, G. J. Martyna, and M. L. Klein, *J. Chem. Phys.* **99**, 2796 (1993).
- [51] H. R. Glyde, S. O. Diallo, R. T. Azuah, O. Kirichek, and J. W. Taylor, *Phys. Rev. B* **84**, 184506 (2011).
- [52] S. Goto, K. Kim, and N. Matsubayashi, *ACS Polymer* **3**, 437 (2023).
- [53] X. Cai, C. Liang, H. Liu, and G. Zhang, *Polymer* **253**, 124953 (2022).
- [54] A. L. Nichols, D. Chandler, Y. Singh, and D. M. Richardson, *J. Chem. Phys.* **81**, 5109 (1984).
- [55] M. Rubinstein and R. H. Colby, *Polymer Physics* (Oxford University Press, NY, 2003).
- [56] V. V. Brazhkin, Y. D. Fomin, A. G. Lyapin, V. N. Ryzhov, E. N. Tsiok, and K. Trachenko, *Phys. Rev. Lett.* **111**, 145901 (2013).
- [57] F. Caupin, S. Balibar, and H. J. Maris, *Physica B* **329-333**, 356 (2003).
- [58] F. Werner, G. Beaume, A. Hobeika, S. Nascimbene, C. Herrmann, F. Caupin, and S. Balibar, *J. Low Temp. Phys.* **136**, 93 (2004).
- [59] E. Tombari, C. Ferrari, G. Salvetti, and G. P. Johari, *J. Chem. Phys.* **123**, 051104 (2005).
- [60] J. K. Hoffer, W. R. Gardner, C. G. Waterfield, and N. E. Phillips, *J. Low Temp. Phys.* **23**, 63 (1976).
- [61] L. Goldstein, *Phys. Rev.* **122**, 726 (1961).
- [62] T. A. Lima, L. F. O. Faria, V. H. Paschoal, and M. C. C. Ribeiro, *J. Chem. Phys.* **148**, 171101 (2018).
- [63] G. P. Johari, *Phys. Chem. Chem. Phys.* **3**, 2483 (2001).
- [64] H. Imaoka and K. Kinugawa, *Chem. Phys. Lett.* **671**, 174 (2017).
- [65] T. Markham, J.-Y. Ji, and E. D. Held, *J. Stat. Mech.* **2020**, 103103 (2020).
- [66] K. Glaum, H. Kleinert, and A. Pelster, *Phys. Rev. A* **76**, 063604 (2007).
- [67] K. Yamamoto, Y. Shibayama, and K. Shirahama, *Phys. Rev. Lett.* **100**, 195301 (2008).
- [68] T. Tani, Y. Nago, S. Murakawa, and K. Shirahama, *J. Phys. Soc. Jpn.* **91**, 014603 (2022).
- [69] F. M. Gasparini, M. O. Kimball, K. P. Mooney, and M. Diaz-Avila, *Rev. Mod. Phys.* **80**, 1009 (2008).
- [70] M. Tsujimoto and K. Kinugawa, to be submitted.
- [71] F. Tanaka, *Phys. Rev. E* **73**, 061405 (2006).
- [72] A. Nakayama and N. Makri, *Proc. Natl. Acad. Sci. U. S. A.* **102**, 4230 (2005).
- [73] M. Boninsegni, N. Prokof’ev, and B. Svistunov, *Phys. Rev. Lett.* **96**, 105301 (2006).
- [74] S. Rastogi, M. Newman, and A. Keller, *Nature* **353**, 55 (1991).
- [75] K. Mortensen, W. Brown, and B. Norden, *Phys. Rev. Lett.* **68**, 2340 (1992).
- [76] K. Shirahama, K. Yamamoto, and Y. Shibayama, *Low Temp. Phys.* **34**, 273 (2008).
- [77] J. Taniguchi, R. Fujii, and M. Suzuki, *Phys. Rev. B* **84**, 134511 (2011).
- [78] J. Bossy, J. Ollivier, H. Schober, and H. R. Glyde, *Phys. Rev. B* **86**, 224503 (2012).
- [79] K. Yamamoto, H. Nakashima, Y. Shibayama, and K. Shirahama, *Phys. Rev. Lett.* **93**, 075302 (2004).

- [80] K. Yamamoto, Y. Shibayama, and K. Shirahama, J. Phys. Soc. Jpn. **77**, 013601 (2008).
 - [81] K. Shirahama, K. Yamamoto, and Y. Shibayama, J. Phys. Soc. Jpn. **77**, 111011 (2008).
 - [82] J. Bossy, J. V. Pearce, H. Schober, and H. R. Glyde, Phys. Rev. Lett **101**, 025301 (2008).
 - [83] J. Taniguchi, Y. Aoki, and M. Suzuki, Phys. Rev. B **82**, 104509 (2010).
 - [84] J. Taniguchi, K. Demura, and M. Suzuki, Phys. Rev. B **88**, 014502 (2013).
 - [85] J. Bossy, J. Ollivier, and H. R. Glyde, Phys. Rev. B **99**, 165425 (2019).
 - [86] S. Balibar and F. Caupin, J. Phys. Condens. Matter **20**, 173201 (2008).
-

SUPPLEMENTARY MATERIAL
of
Two liquid states of distinguishable helium-4: the existence of another non-superfluid
frozen by heating

Momoko Tsujimoto and Kenichi Kinugawa

Department of Chemistry, Graduate School of Humanities and Sciences, Nara Women's University, Nara 630-8506, Japan

PART A. SUPPLEMENTARY FIGURES

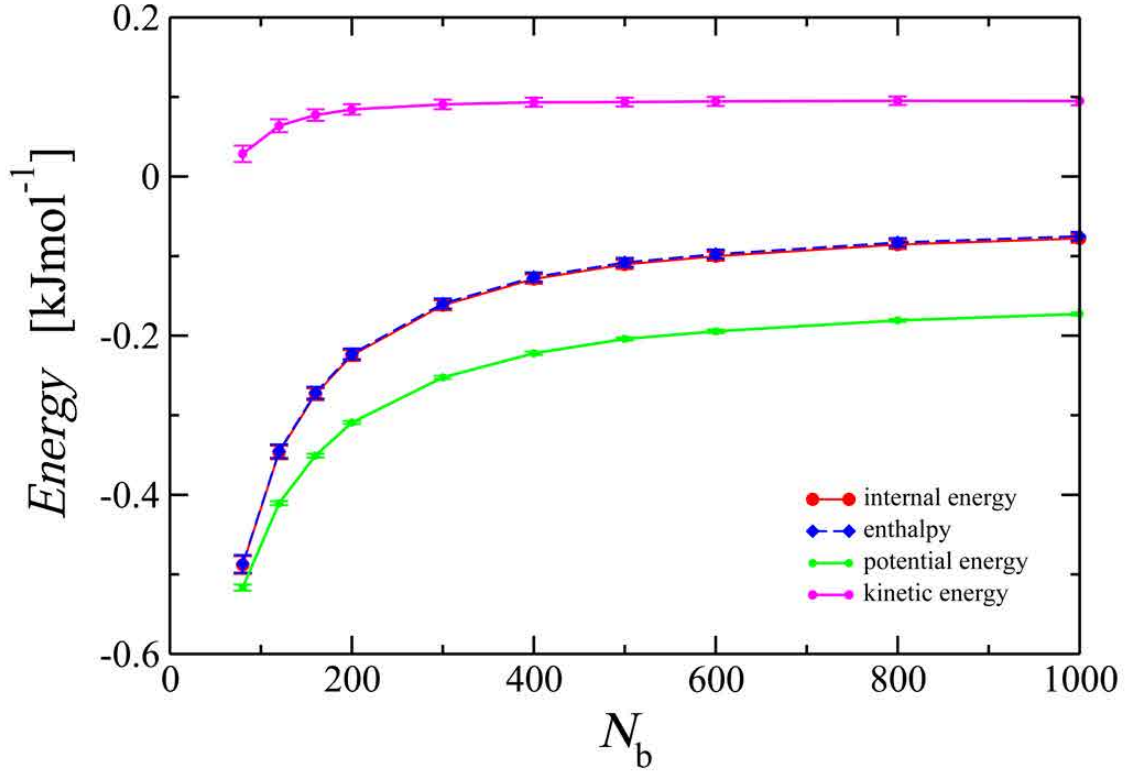


FIG. SA-1. The Trotter number dependence of energetic properties. This test was carried out for the canonical ensemble at 0.1 K and SVP density (0.145 gcm^{-3}) spanning 100,000 steps.

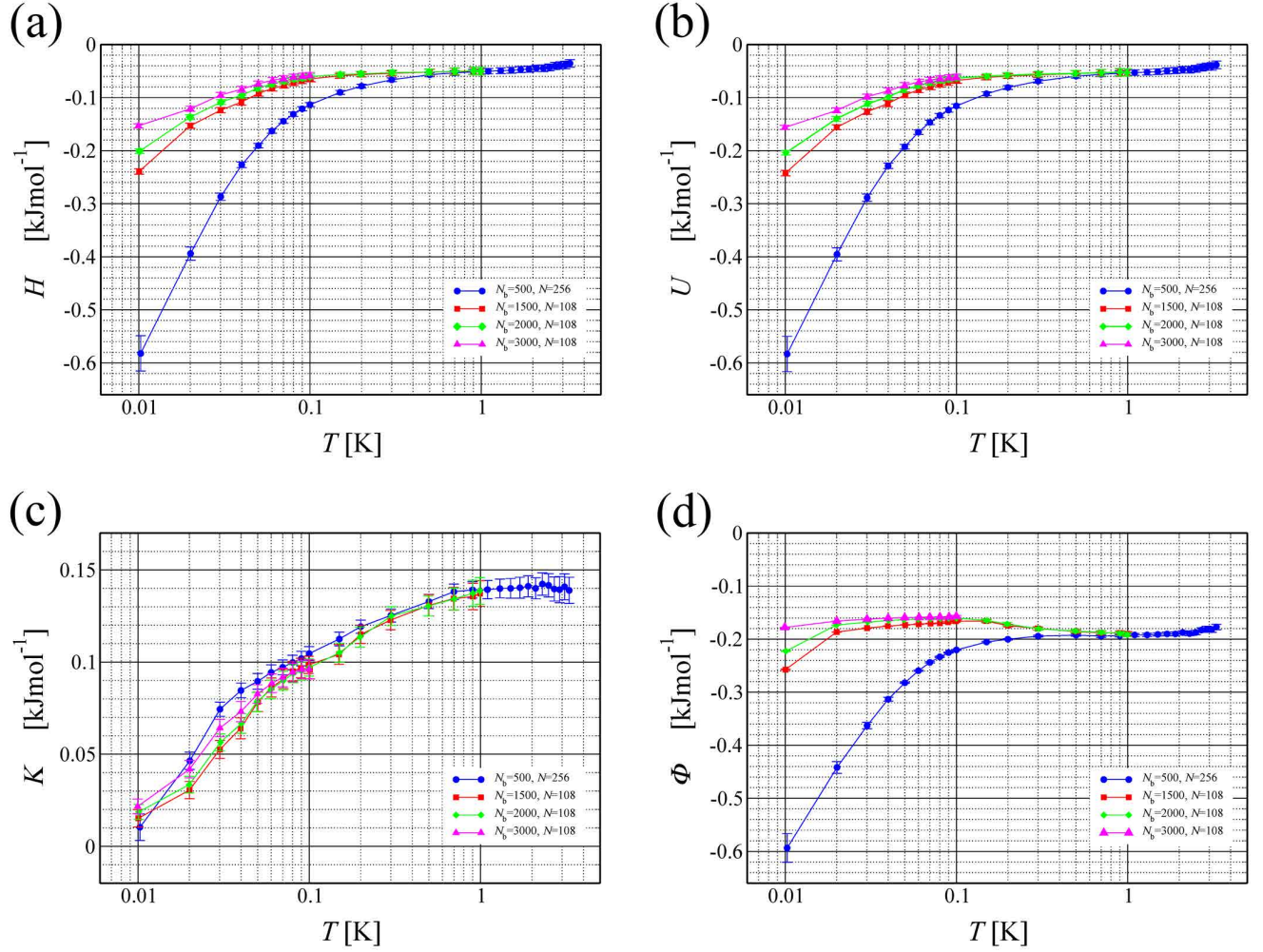


FIG. SA-2. The temperature dependence of the system energetic properties with different Trotter numbers. (a) enthalpy; (b) internal energy; (c) kinetic energy; (d) potential energy; (e) enlarged plot of enthalpy and kinetic energy for 0.01-0.2 K. All the results were obtained from the isobaric-isothermal CMD simulations at 1 bar and each temperature. In (e), we can see slight inflection points of the curves for $N_b = 3000$ at about 0.02 K.

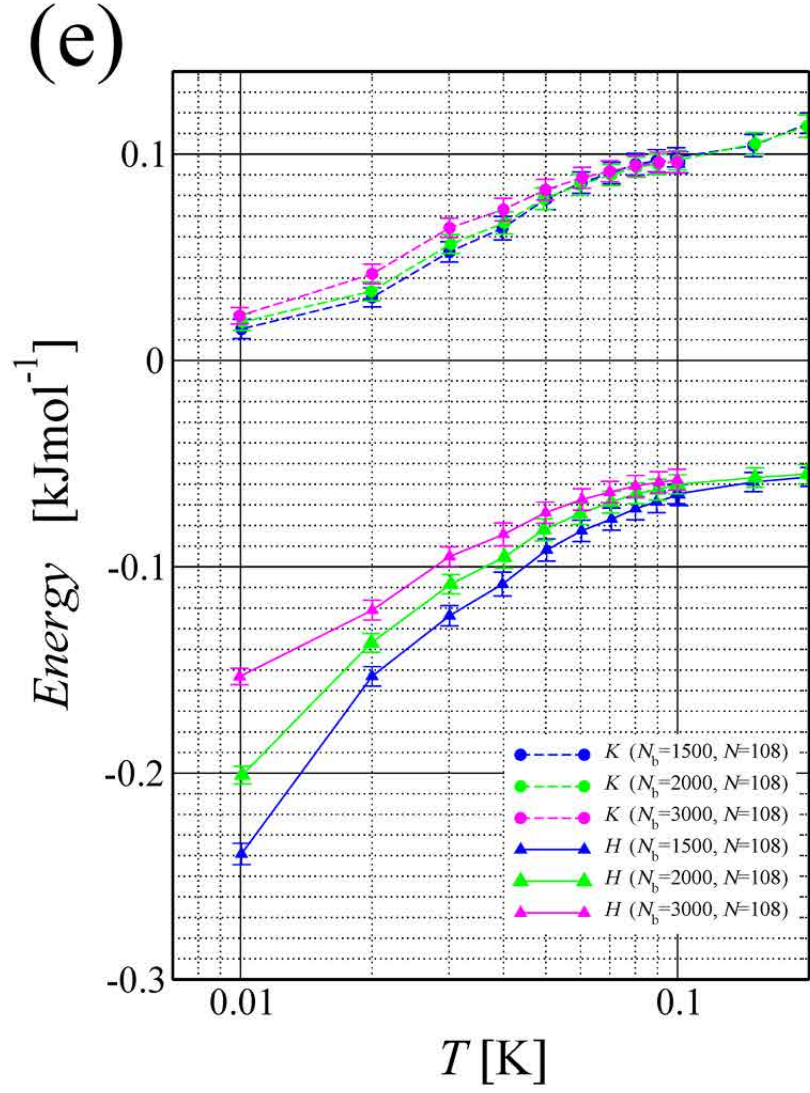


FIG. SA-2. (continued) The temperature dependence of the system energetic properties with different Trotter numbers.

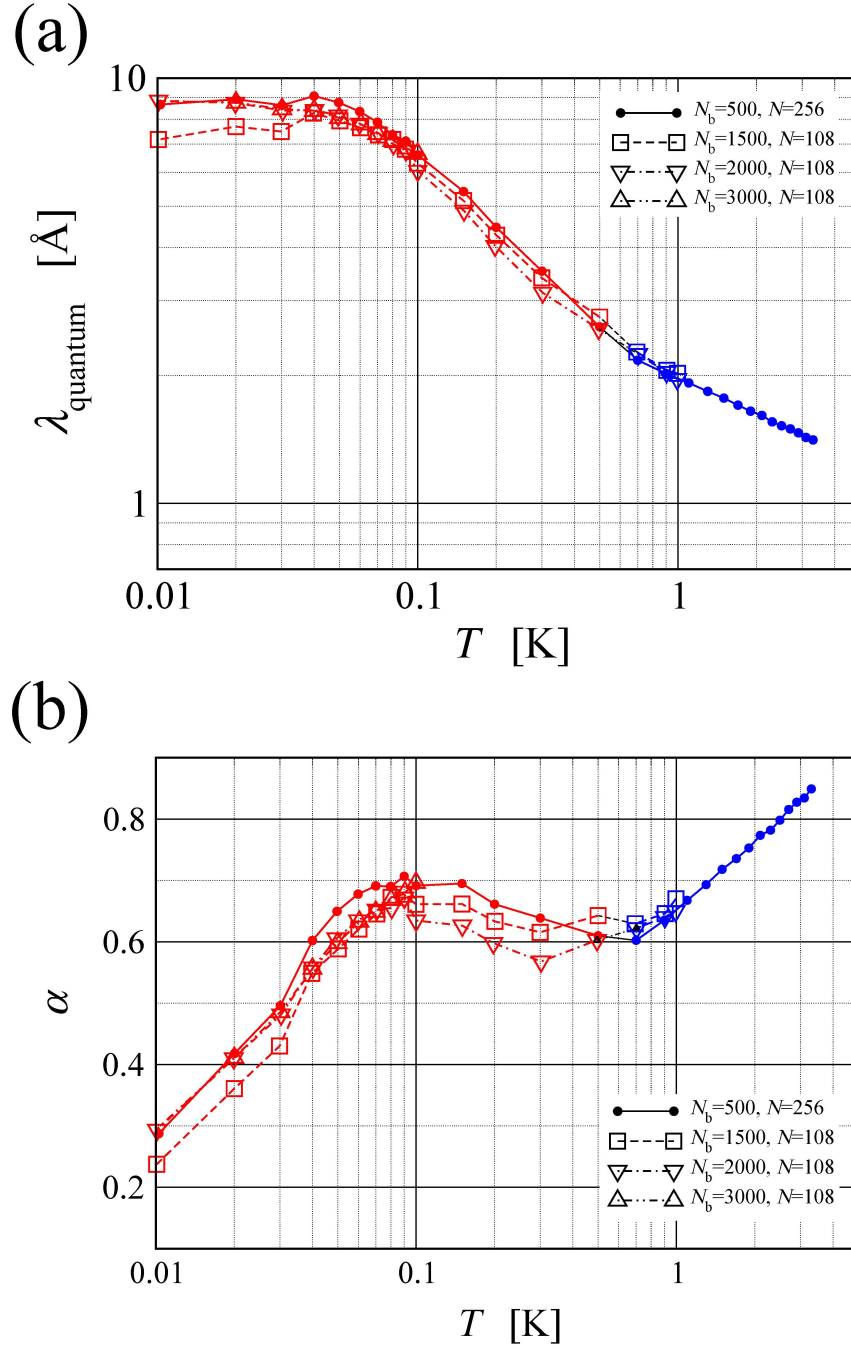


FIG. SA-3. The temperature dependence of quantum wavelength and expansion factor with different Trotter numbers at 1 bar. (a) quantum wavelength; (b) expansion factor. The color of the symbols is the same as that displayed in FIG. 7 and FIG. 8 in the main text: LQDL (blue) and HQDL (red). The definition of these properties is given in Sec. III D. The plotted results of $N_b = 500$ and $N = 256$ involve the 1 bar data shown in FIG. 7 and FIG. 8(a) in the main text.

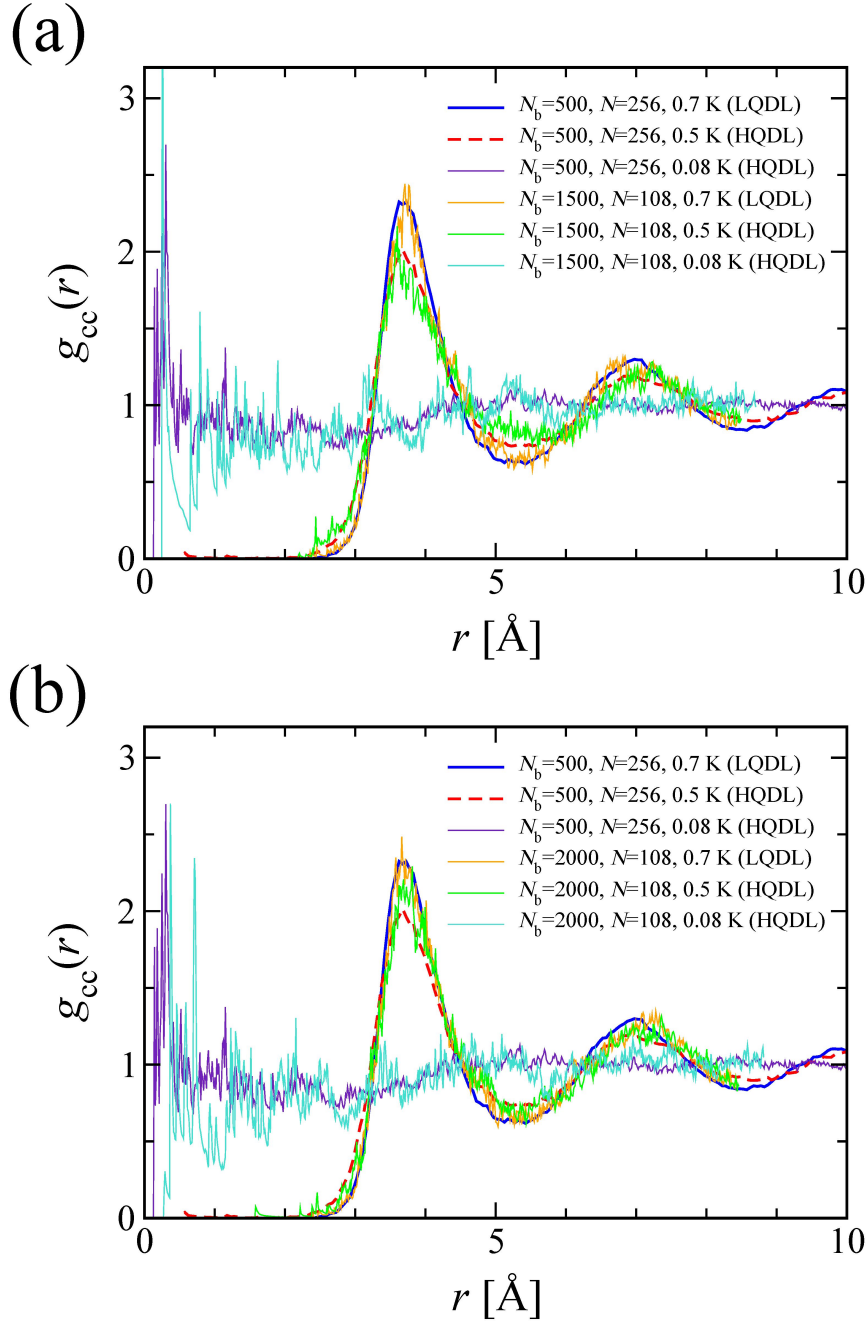


FIG. SA-4. The bead-bead radial distribution function with different Trotter numbers at 1 bar. (a) comparison between $N_b = 500$ and $N_b = 1500$. (b) comparison between $N_b = 500$ and $N_b = 2000$. The plotted results of $N_b = 500$ and $N = 256$ involve the 1 bar data shown in FIG. 6(b) in the main text. We can see that the transition between the LQDL and HQDL occurs between 0.7 and 0.5 K for all N_b conditions.

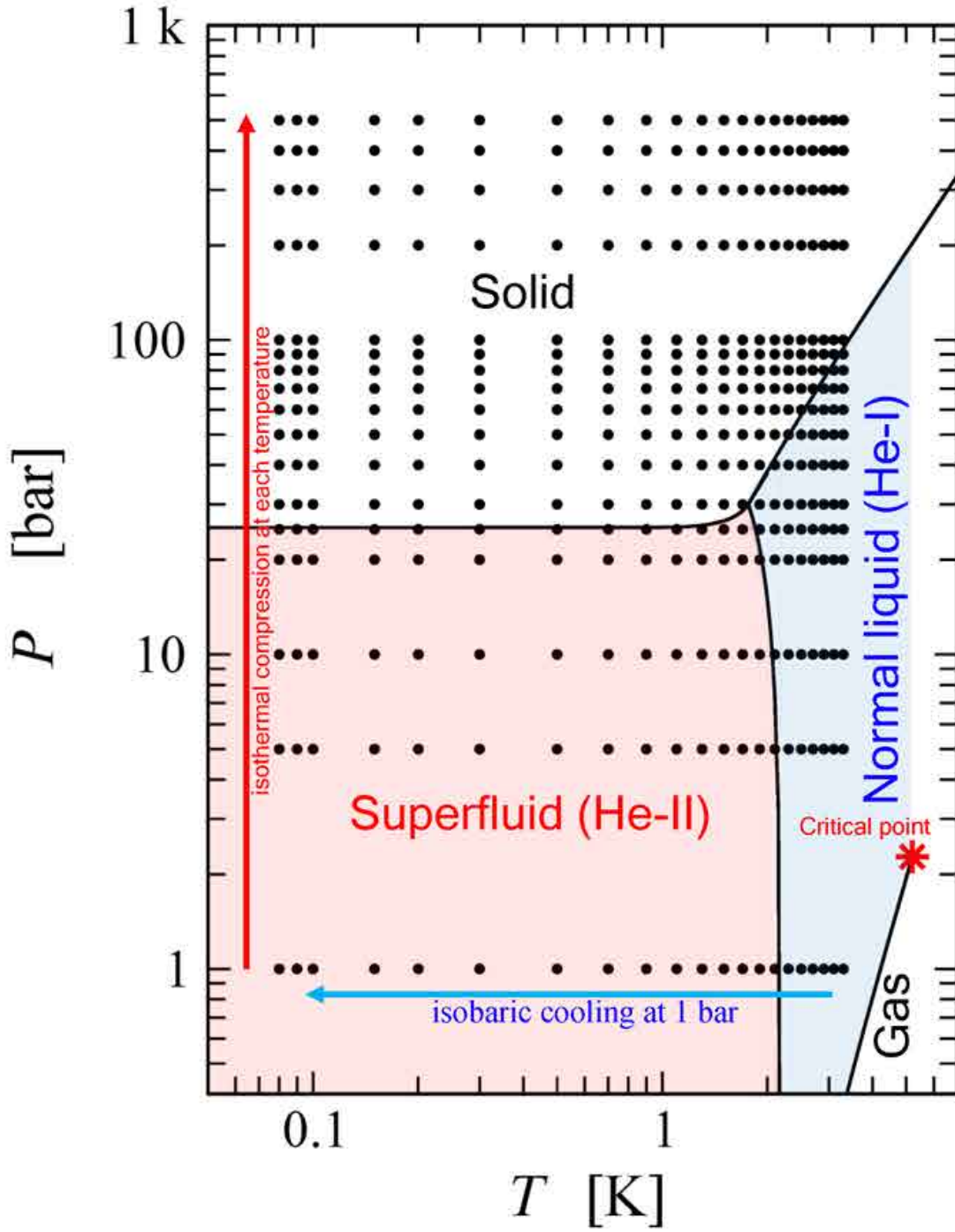


FIG. SA-5. The P - T conditions set for the CMD simulations. The black dots denote 357 conditions (21 temperatures times 17 pressures). The shown phases are experimental ones. Before conducting isothermal compression simulations, the isobaric cooling was conducted at 1 bar to generate the equilibrium state at each temperature at 1 bar.

FIG. SA-6. Schematic representation of CMD procedure. (a) Isobaric cooling run at 1 bar conducted prior to starting the isothermal compression; (b) Isothermal compression run started from each temperature point at 1 bar.

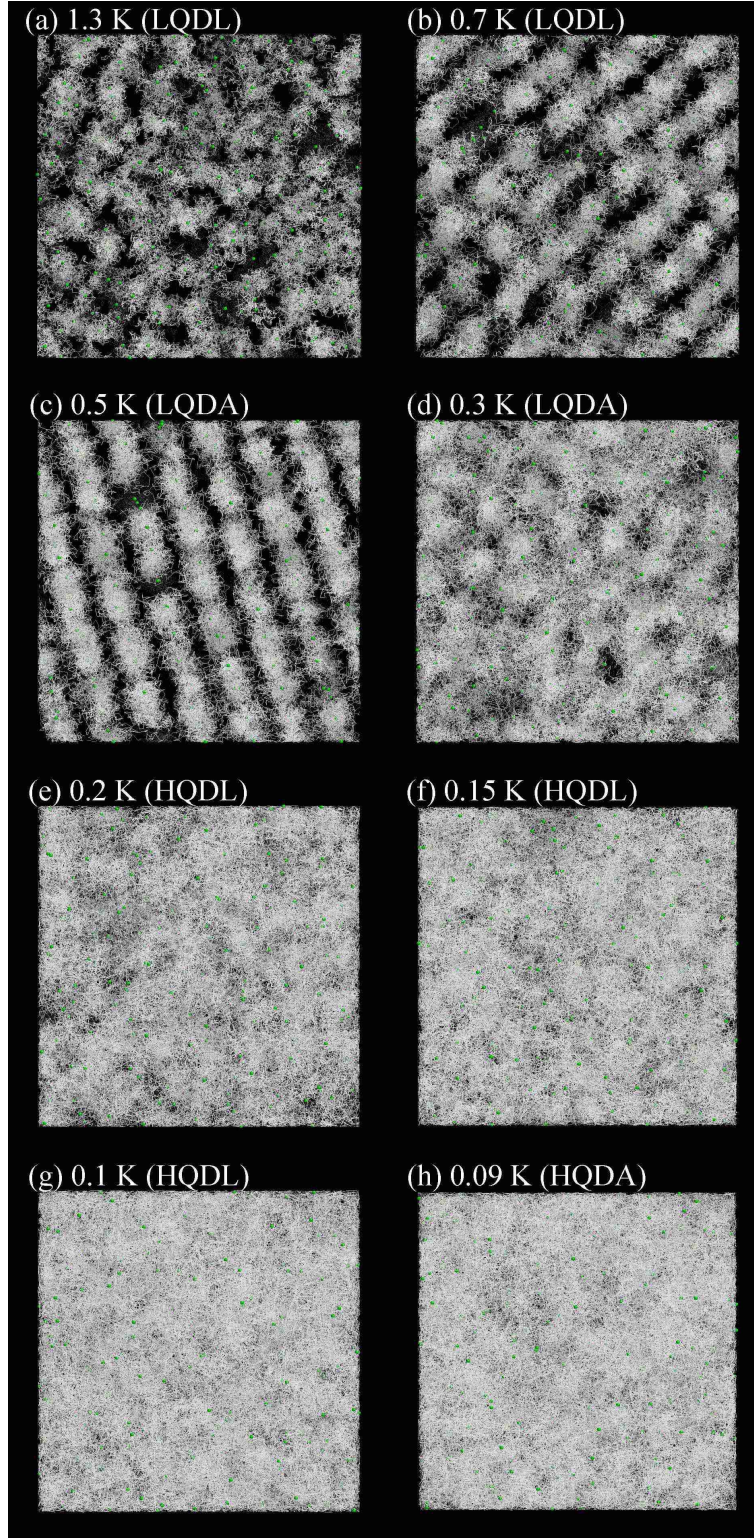


FIG. SA-7. The xy -projected snapshots of the configurations of the ^4He atomic necklaces and centroids at 40 bar. Green spheres and white ones denote the centroids and the beads, respectively. The drawn scales of the centroids and the beads are arbitrary.

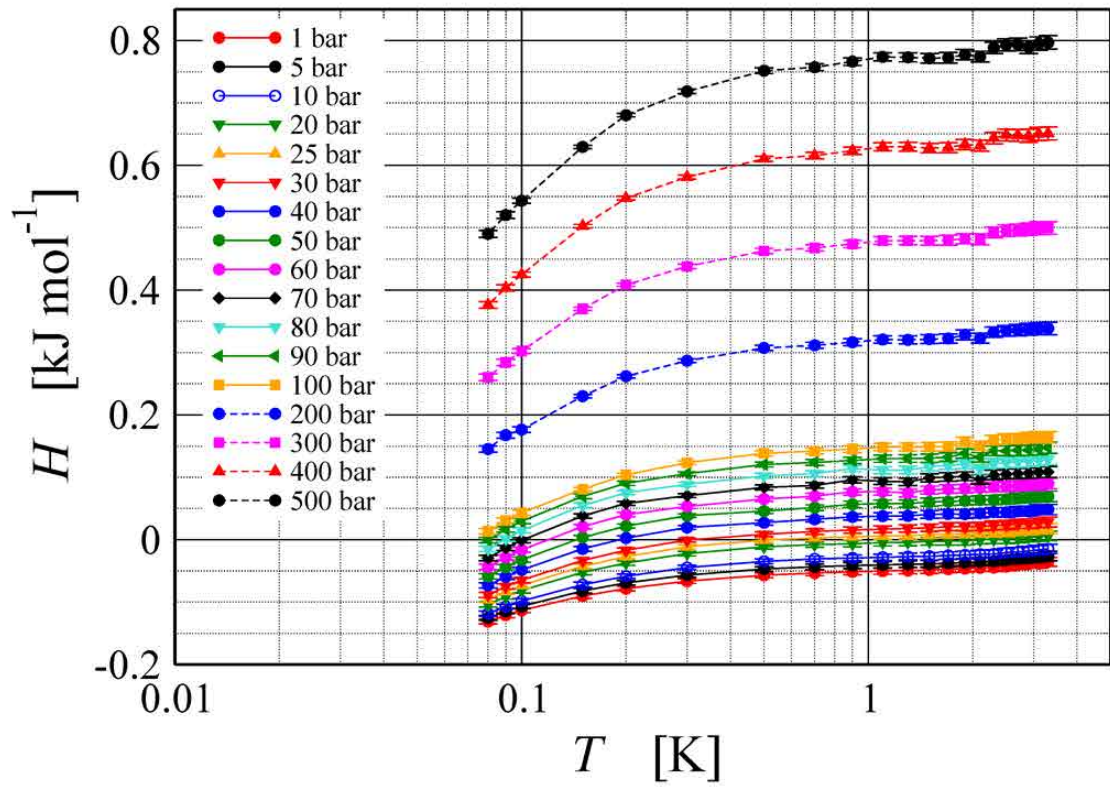


FIG. SA-8. The plot of enthalpy versus temperature over the whole pressure range.

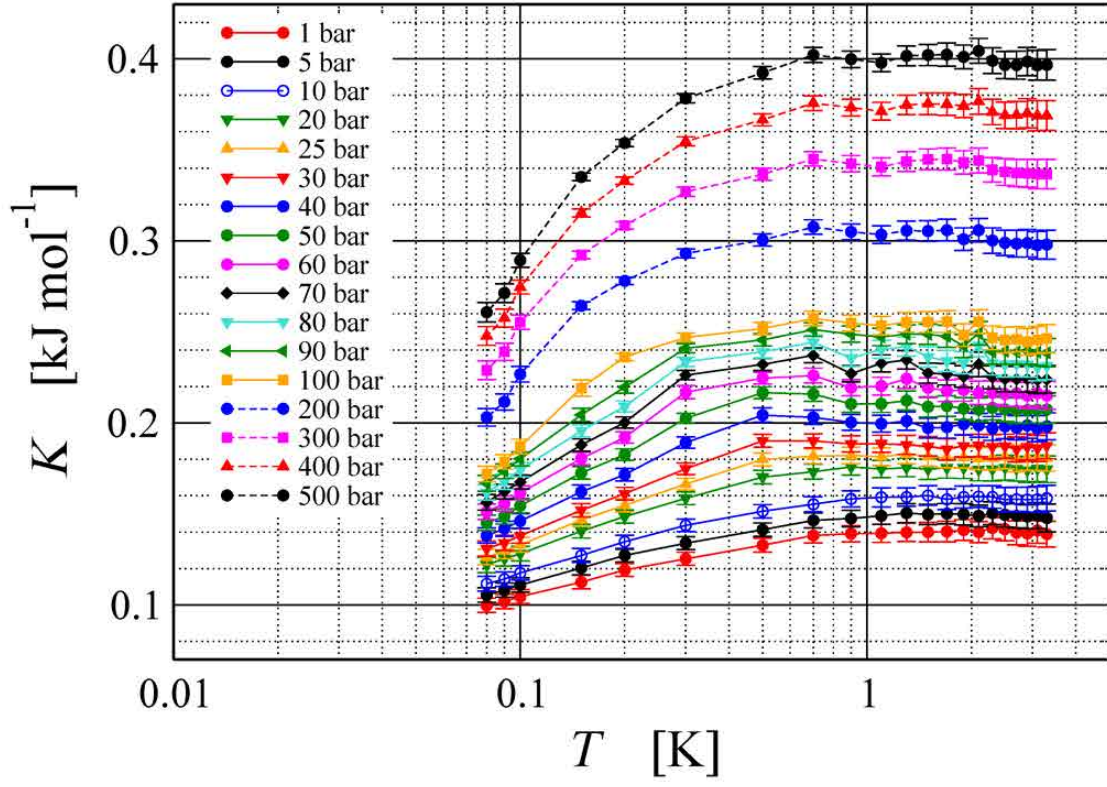


FIG. SA-9. The plot of kinetic energy versus temperature.

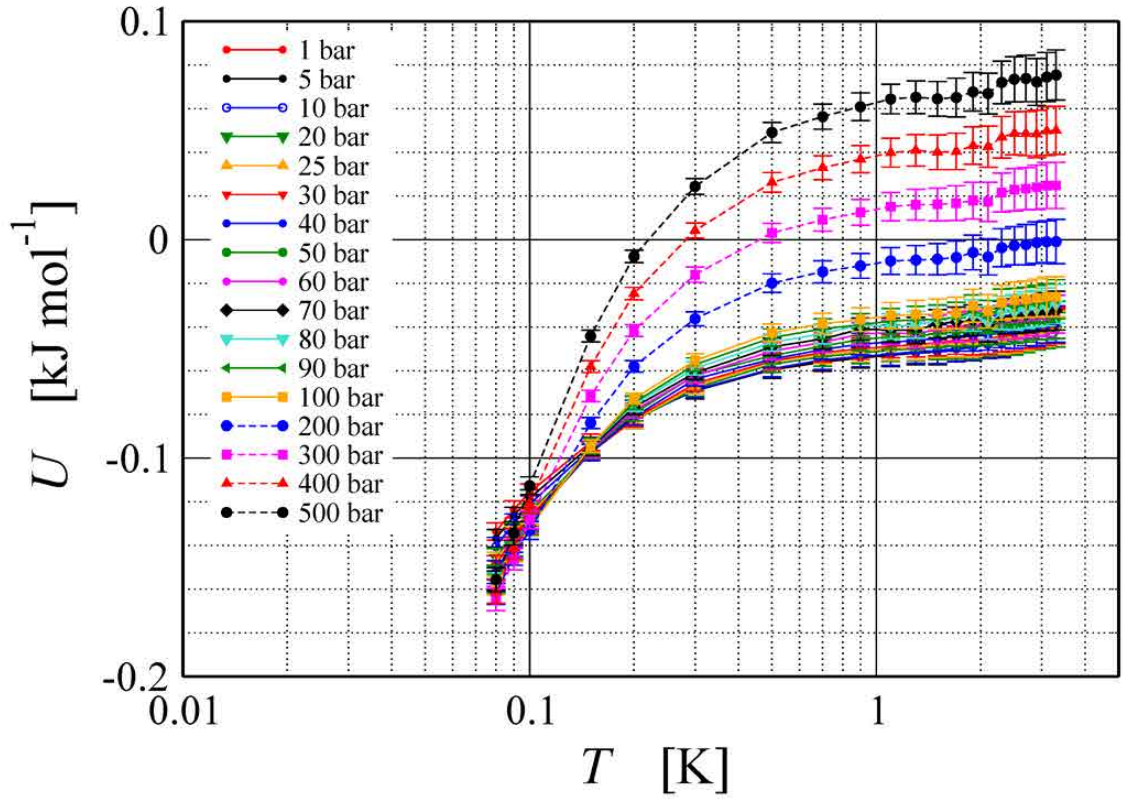


FIG. SA-10. The plot of internal energy versus temperature.

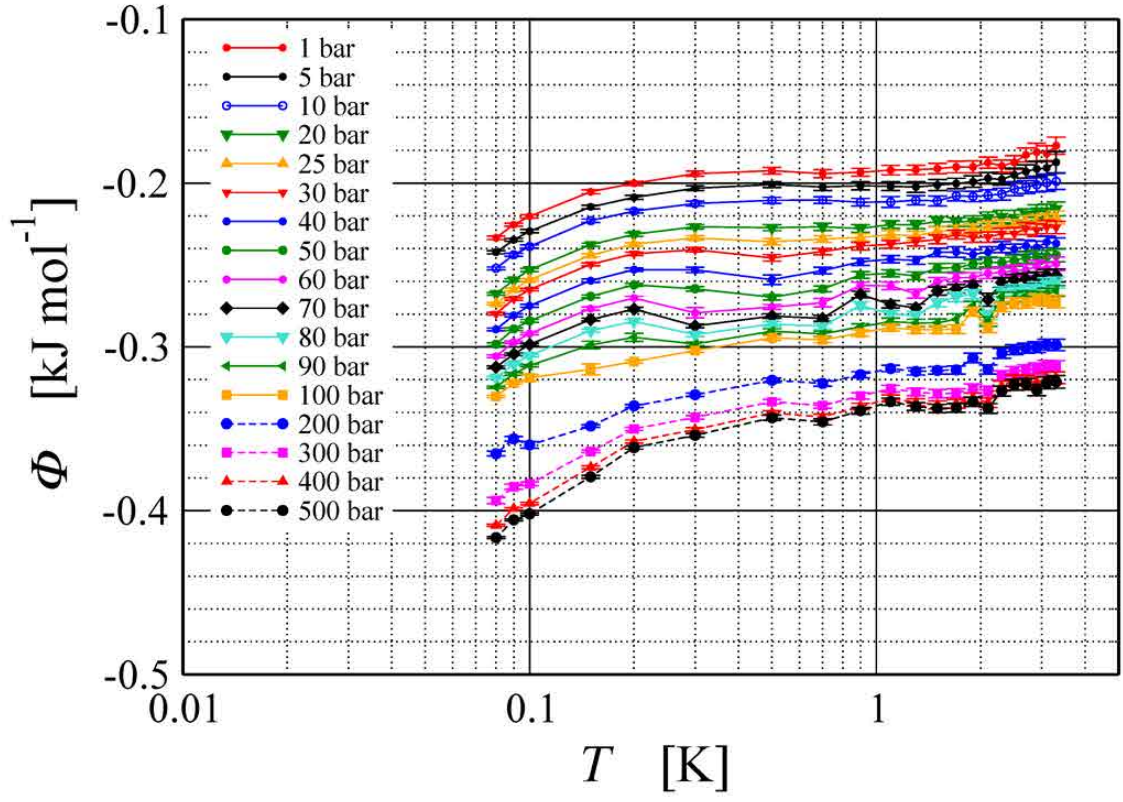


FIG. SA-11. The plot of potential energy versus temperature.

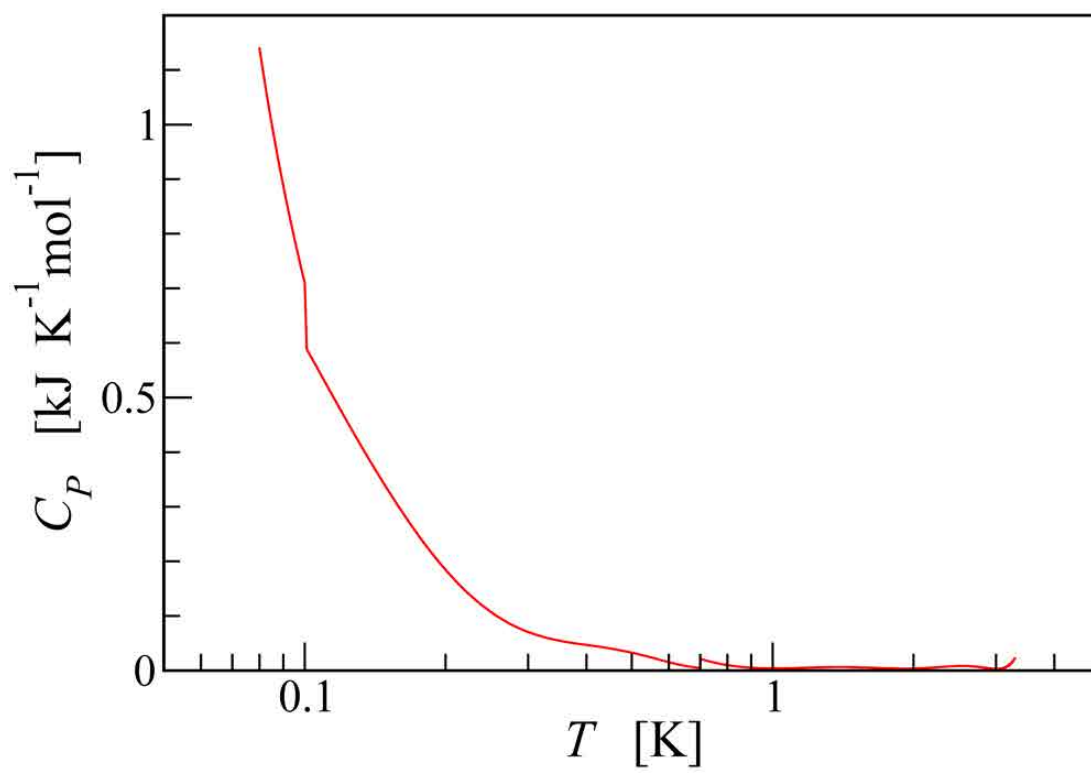


FIG. SA-12. The isobaric heat capacity obtained from the polynomial curve fitting of enthalpy-temperature relation at 1 bar.

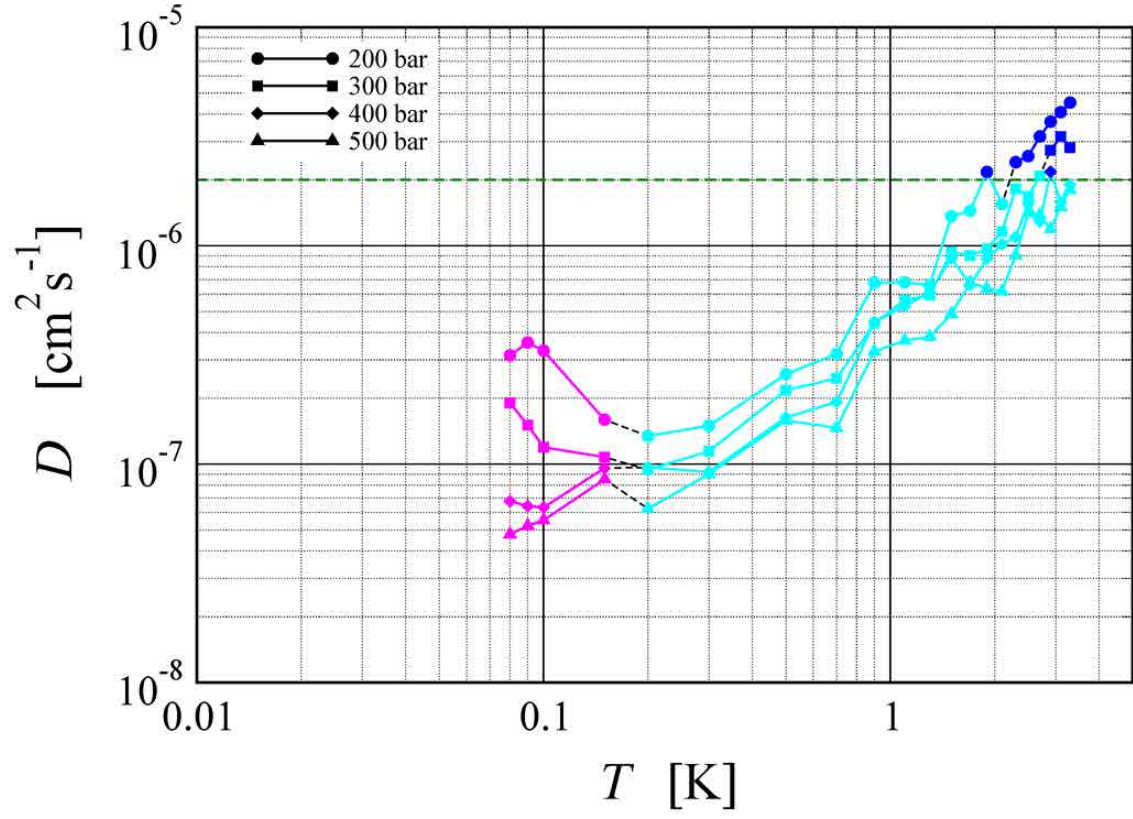


FIG. SA-13. The temperature dependence of apparent self-diffusion coefficient above 200 bar. The colors of the symbols are the same as those displayed in Fig. 1 in the main text: LQDL (blue), LQDA (cyan), HQDL (red), and HQDA (magenta). Green horizontal dashed line denotes the threshold between liquids and glasses.

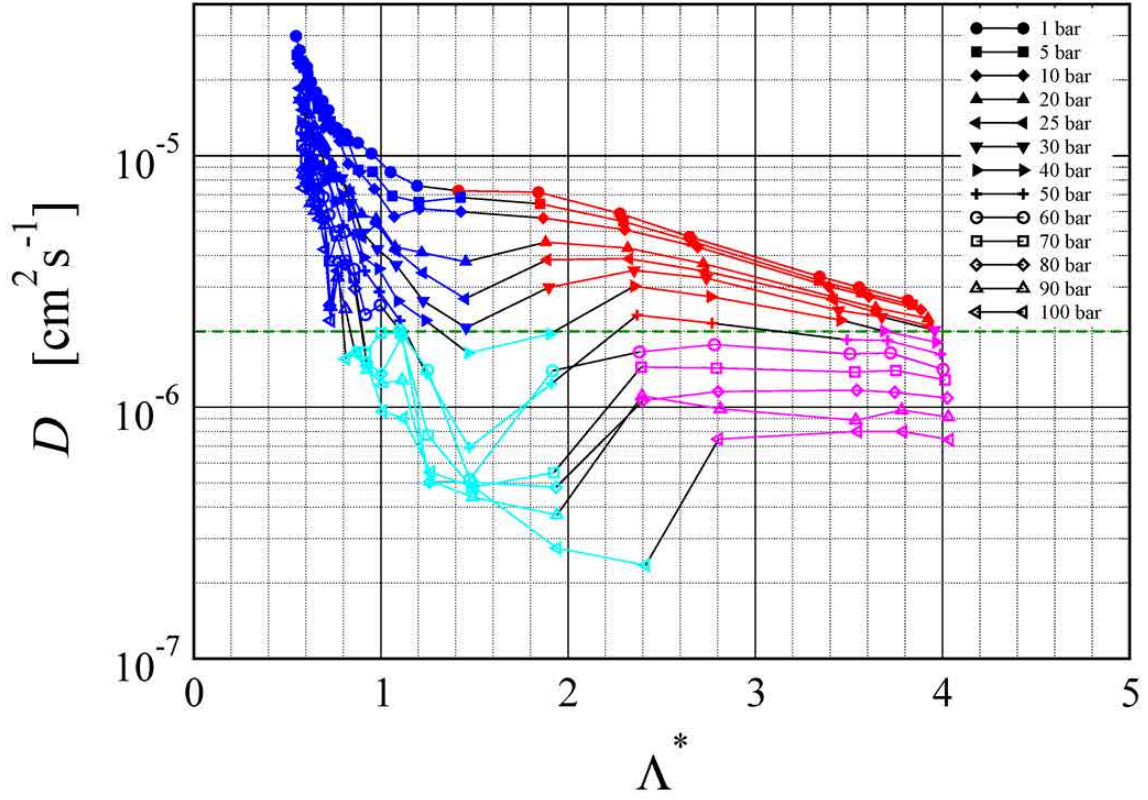


FIG. SA-14. The quantumness parameter dependence of apparent self-diffusion coefficient below 100 bar. The colors of the symbols are the same as those displayed in Fig. 1 in the main text: LQDL (blue), LQDA (cyan), HQDL (red), and HQDA (magenta). Green horizontal dashed line denotes the threshold between liquids and glasses.

PART B. COMPLETE SET OF RADIAL DISTRIBUTION FUNCTIONS AND MEAN SQUARE DISPLACEMENTS

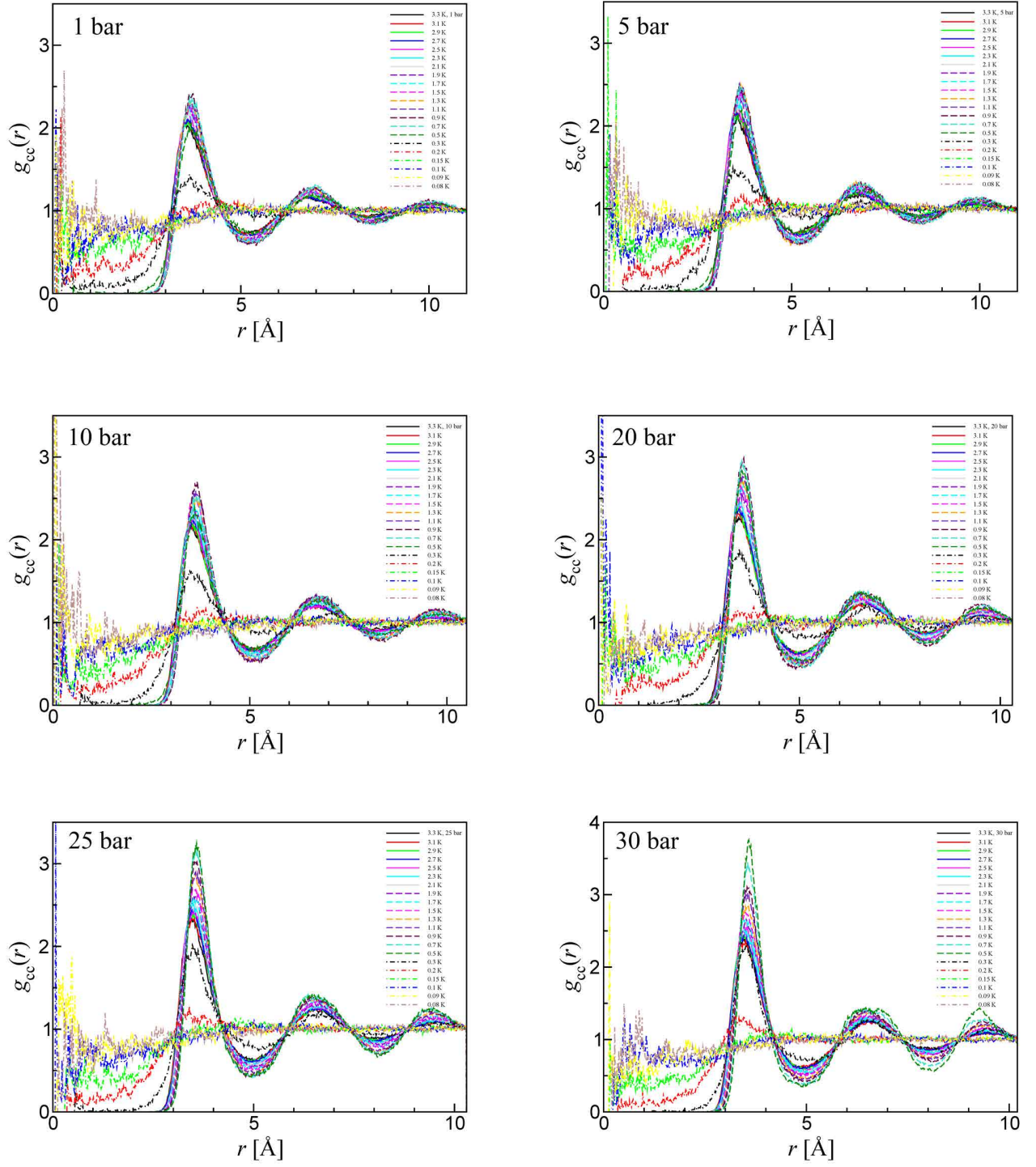


FIG. SB-1. The centroid-centroid radial distribution functions.

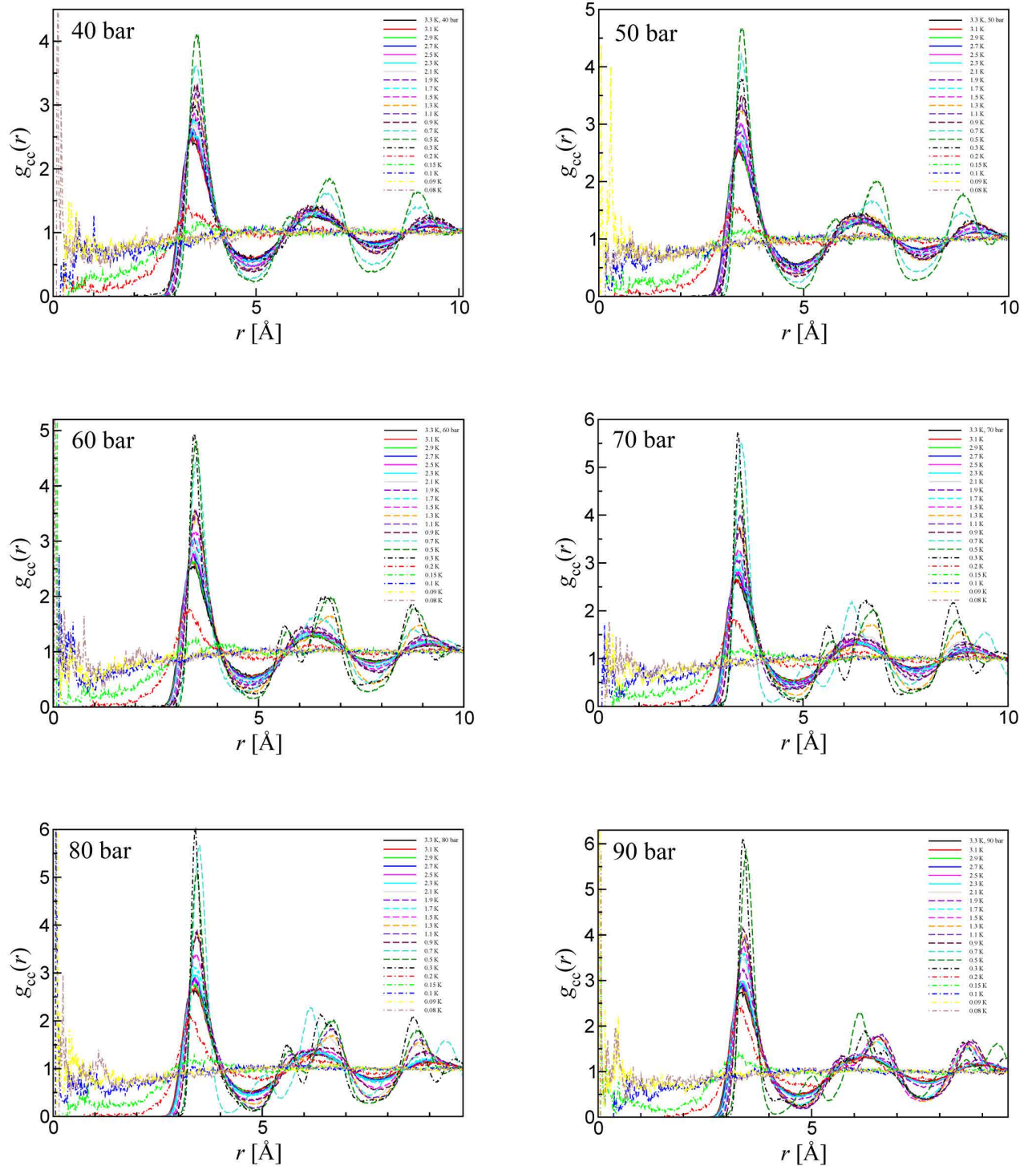


FIG. SB-1. (continued) The centroid-centroid radial distribution functions.

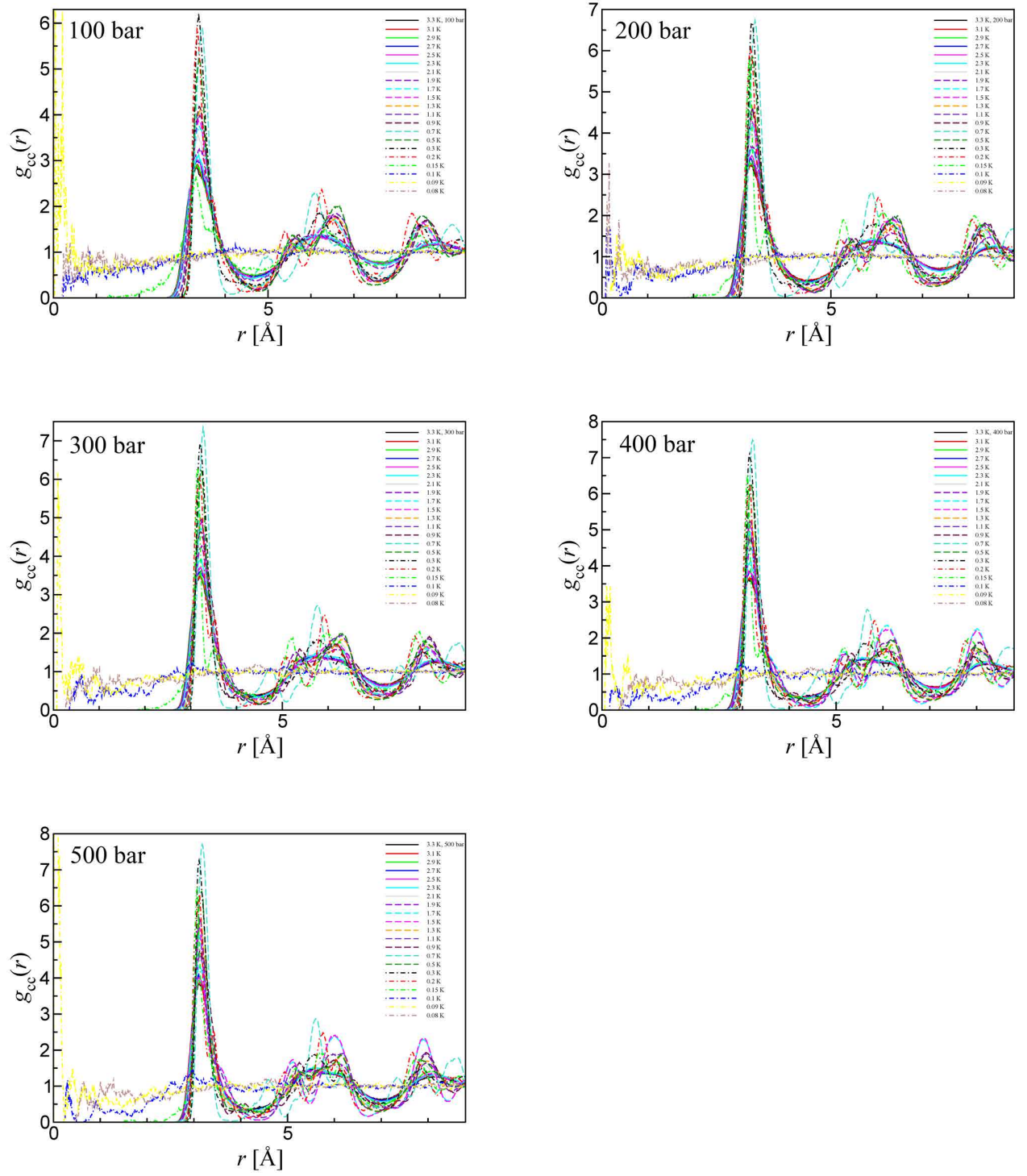


FIG. SB-1. (continued) The centroid-centroid radial distribution functions.

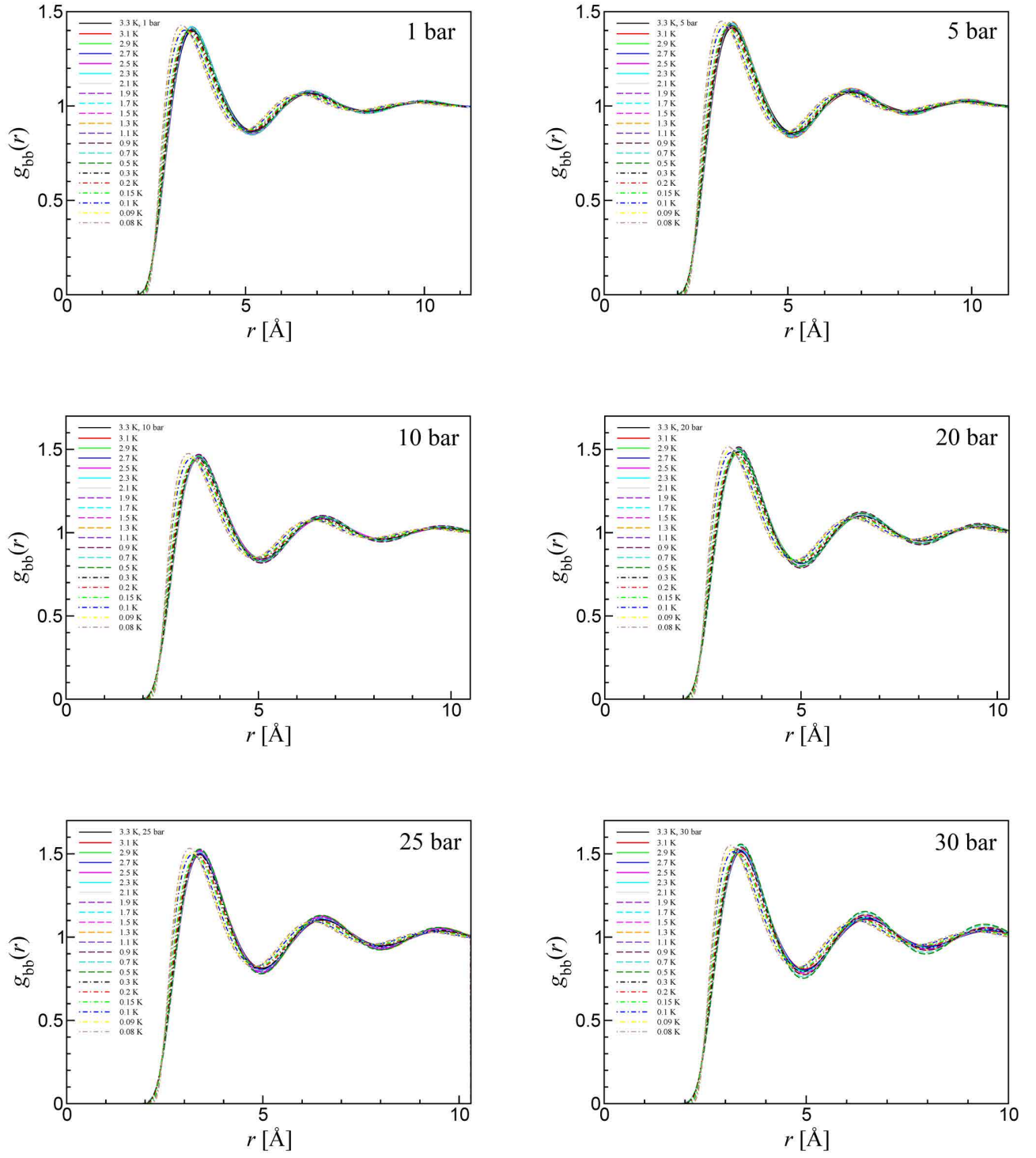


FIG. SB-2. The bead-bead radial distribution functions.

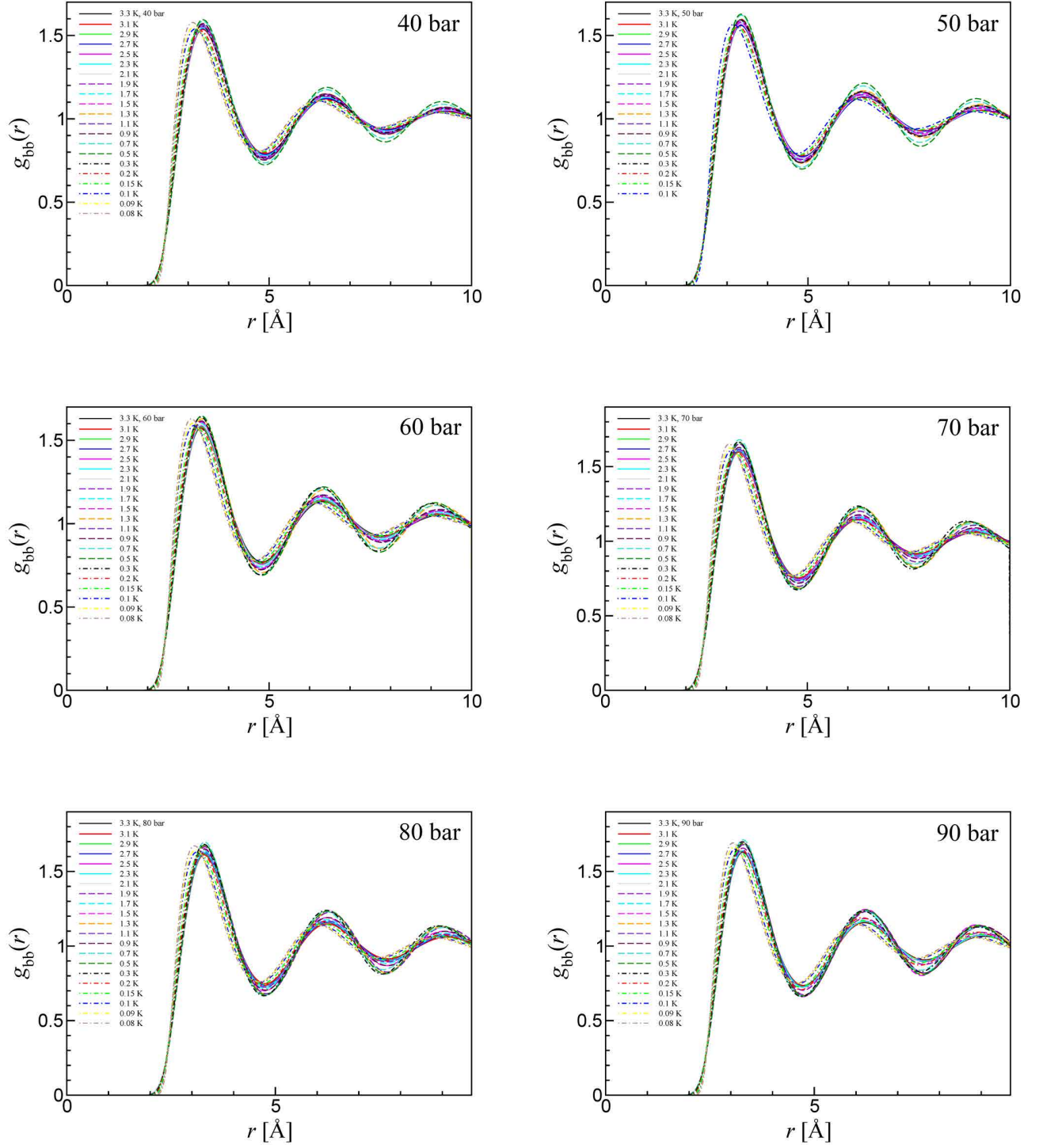


FIG. SB-2. (continued) The bead-bead radial distribution functions.

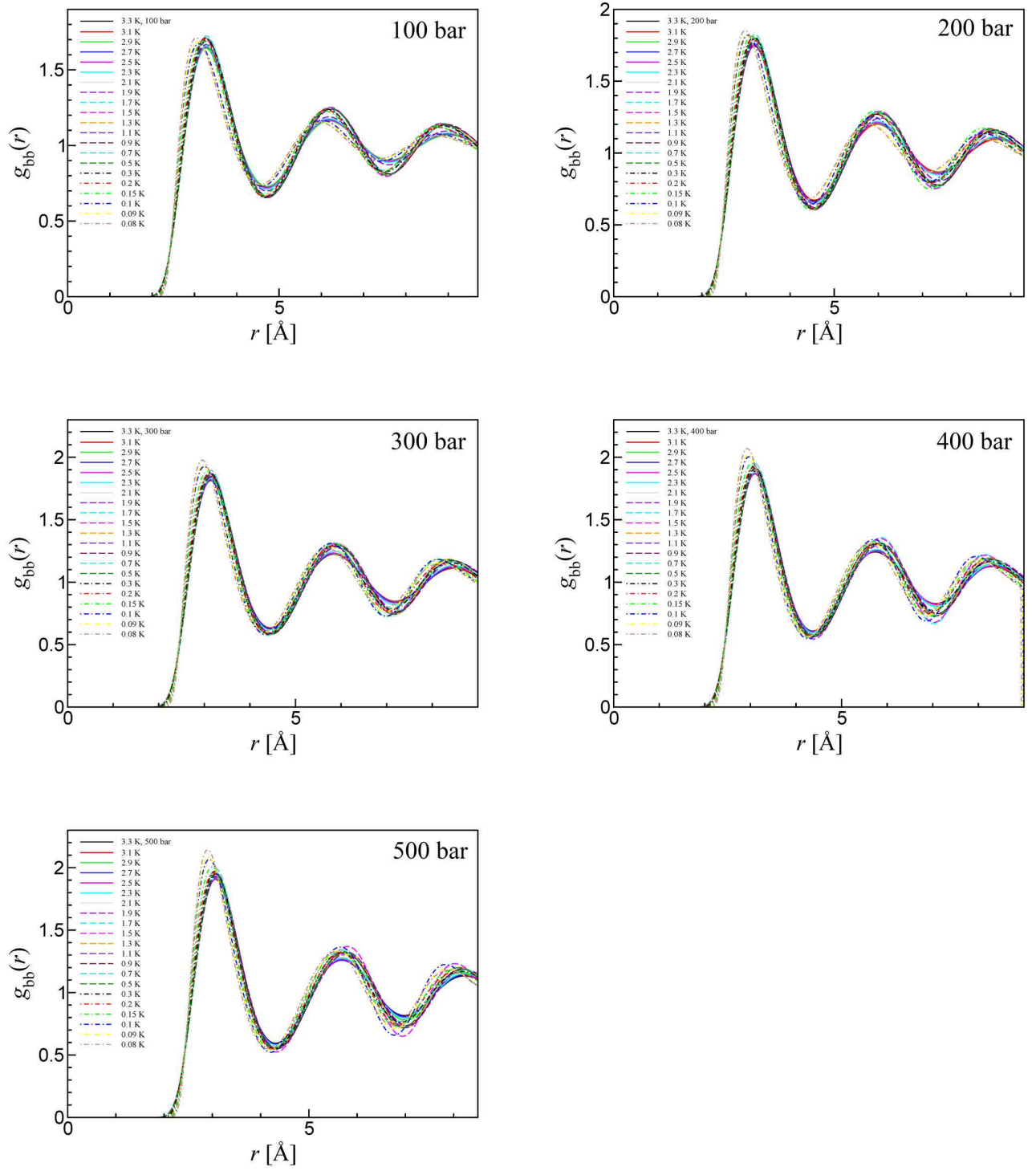


FIG. SB-2. (continued) The bead-bead radial distribution functions.

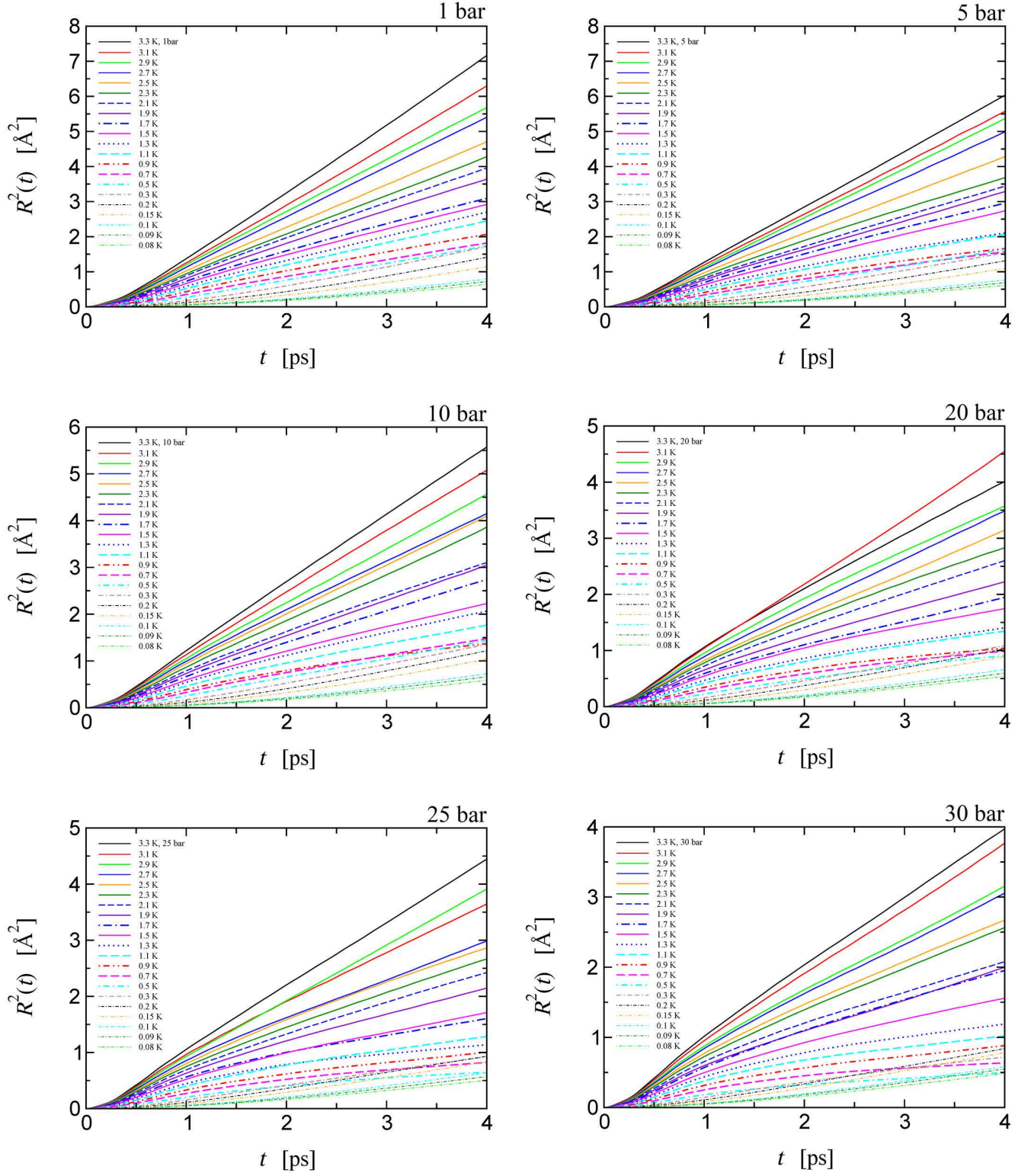


FIG. SB-3. Mean square displacement of atomic centroids.

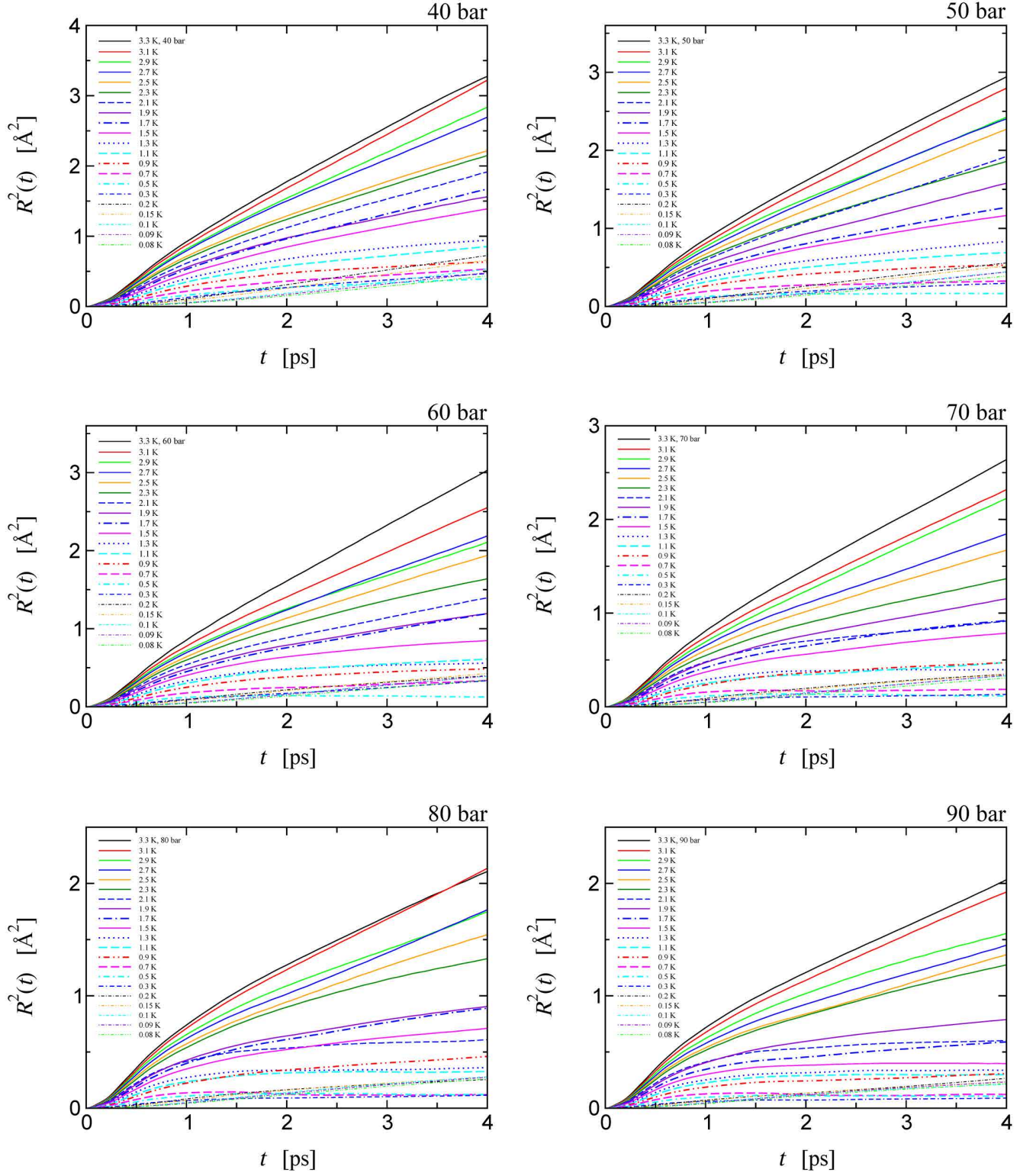


FIG. SB-3. (continued) Mean square displacement of atomic centroids.

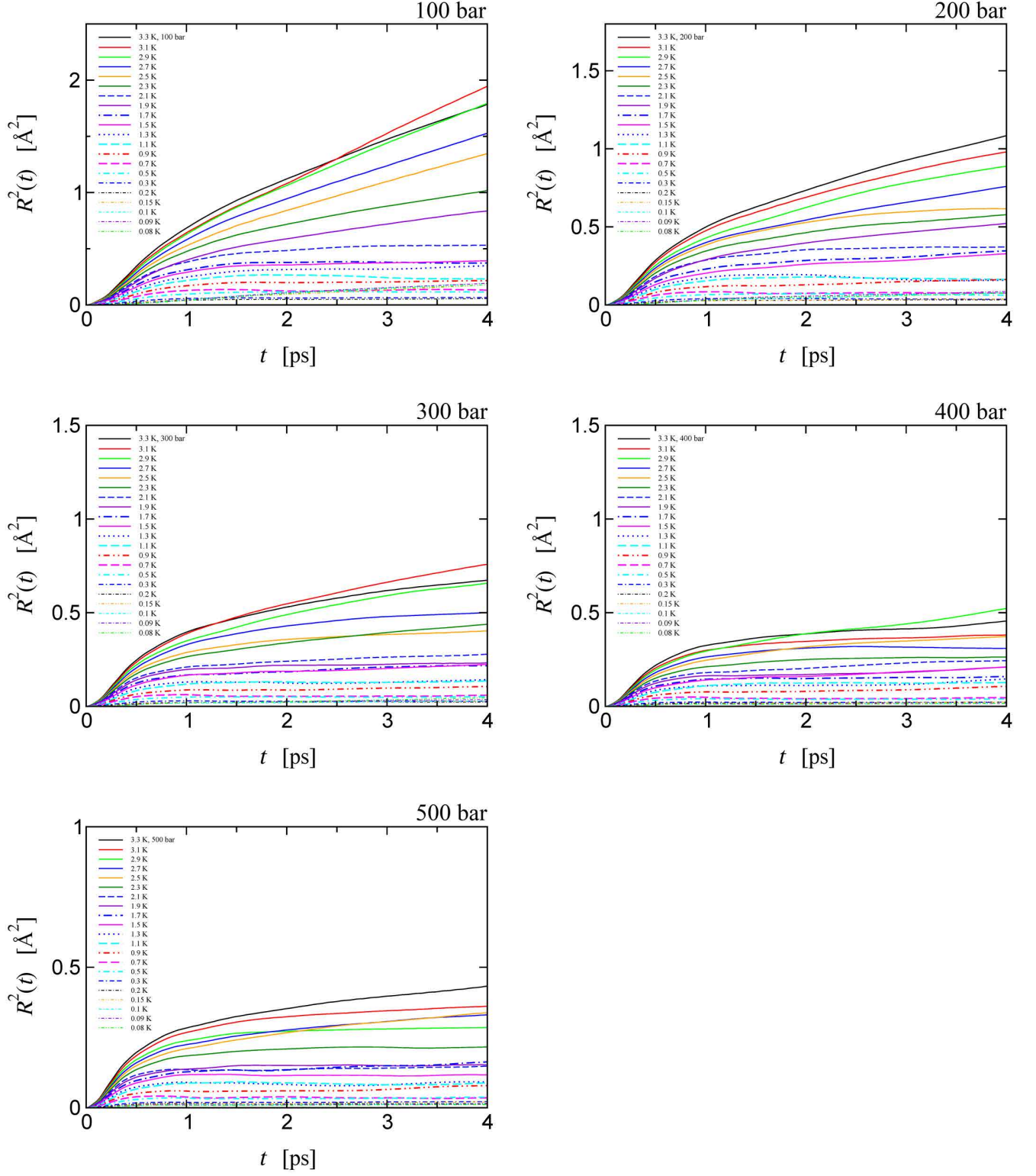


FIG. SB-3. (continued) Mean square displacement of atomic centroids.

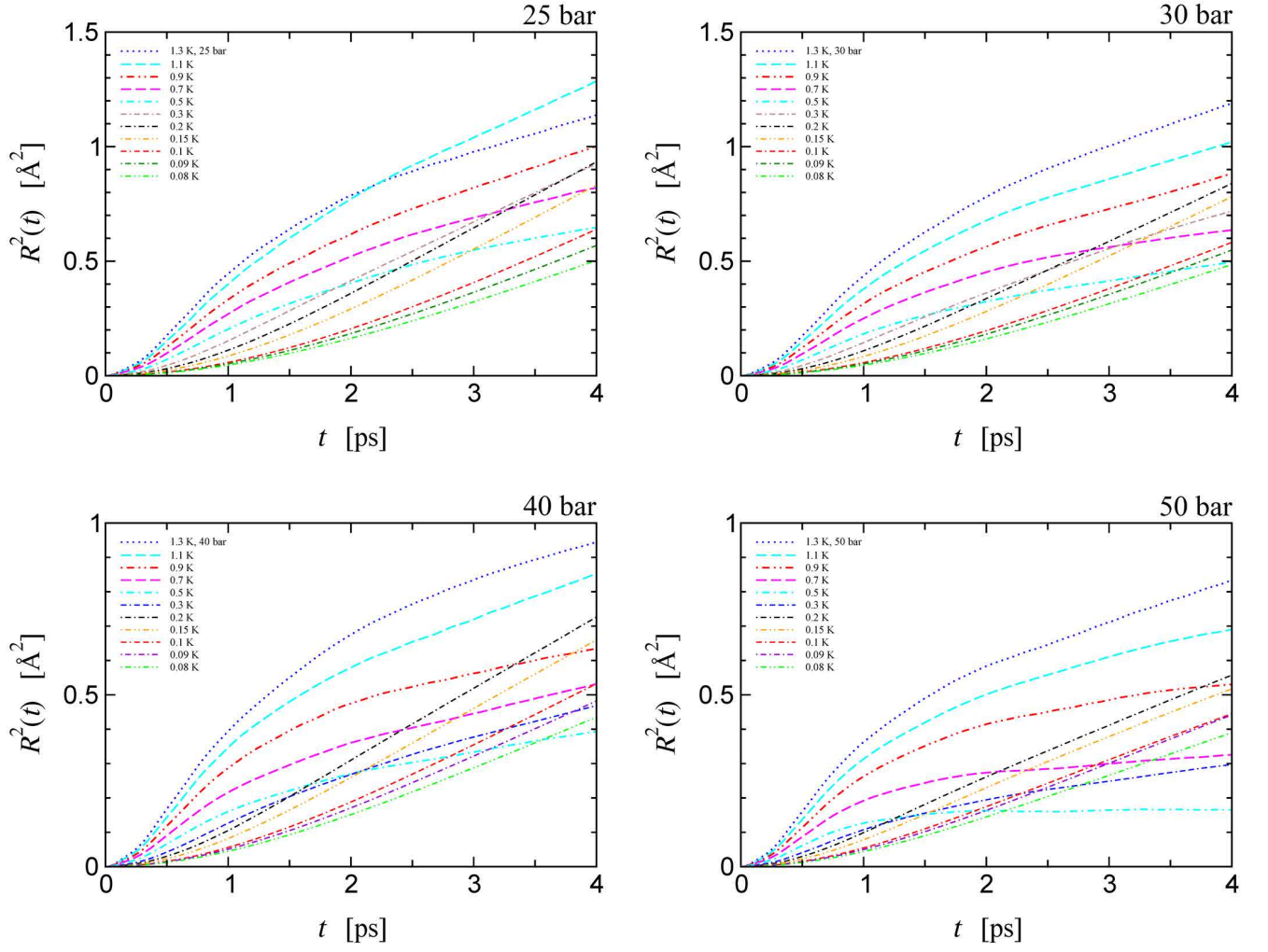


FIG. SB-4. Enlarged plot of mean square displacement of atomic centroids.

PART C. SUPPLEMENTARY DATA OF THE TEST SIMULATION OF INVERSE FREEZING

TABLE SC- I. The averaged properties before and after the state transitions by isobaric heating test at 40 bar.

Property X	0.2 K (HQDL)	0.3 K (LQDA, partially crystallized)	0.4 K (LQDA, partially crystallized)	Increment ΔX from 0.2 K to 0.3 K
U [Jmol ⁻¹]	-80.8	-64.6	-57.6	16.2
K [Jmol ⁻¹]	173.0	197.0	200.3	24.0
Φ [Jmol ⁻¹]	-253.8	-261.6	-257.9	-7.8
H [Jmol ⁻¹]	2.8	17.0	24.6	14.2
V [cm ³ mol ⁻¹]	20.89	20.40	20.56	-0.49
λ_{quantum} [Å]	3.47	1.84	1.68	-1.63
α	0.514	0.334	0.353	-0.180

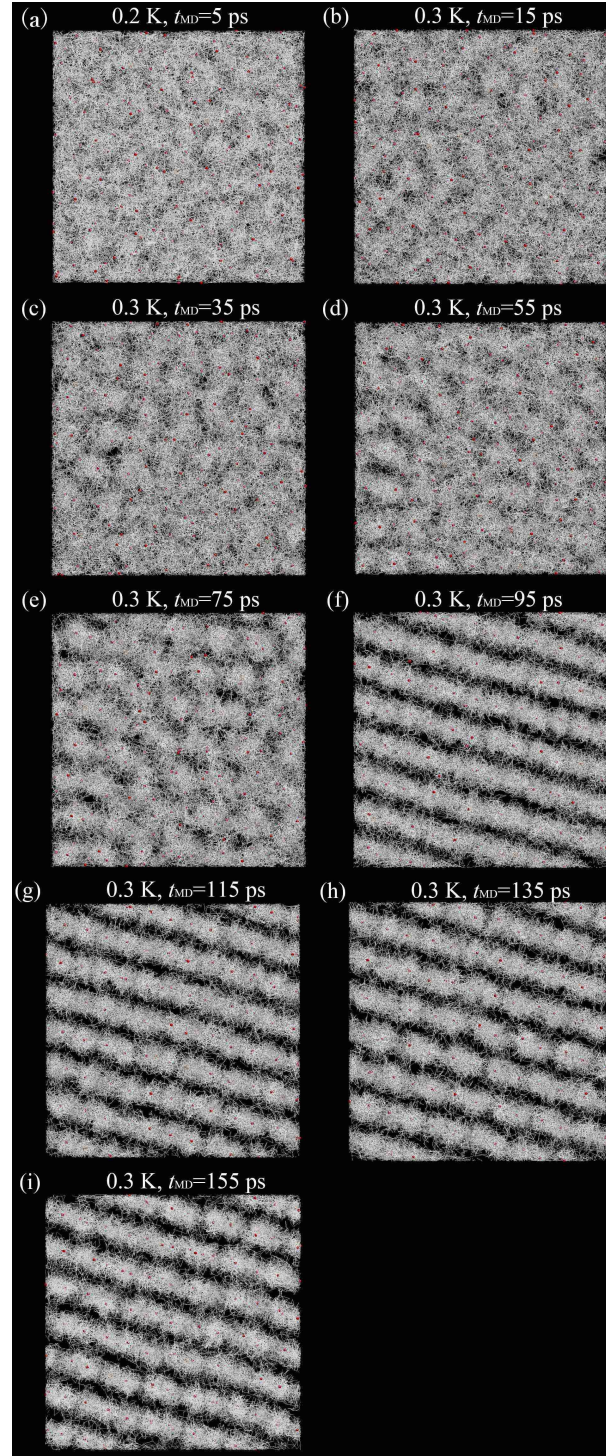


FIG. SC-1. The xy -projected snapshots of the configuration of the ^4He atomic necklaces and centroids during the process of isobaric heating from 0.2 K to 0.3 K at 40 bar.